# TACTICAL MISSILE PERFORMANCE FOR SINGLE AND MULTI-WIRE EMBEDDED PROPELLANT CONFIGURATIONS WITH DISCONTINUITIES

THESIS

Paul B. Wilson, Captain, USAF

AFIT-ENY-MS-19-M-253

**DEPARTMENT OF THE AIR FORCE**
**AIR UNIVERSITY**

## AIR FORCE INSTITUTE OF TECHNOLOGY

**Wright-Patterson Air Force Base, Ohio**

AFIT-ENY-MS-19-M-253

# TACTICAL MISSILE PERFORMANCE FOR SINGLE AND MULTI-WIRE EMBEDDED PROPELLANT CONFIGURATIONS WITH DISCONTINUITIES

THESIS

Presented to the Faculty

Department of Aeronautics and Astronautics

Graduate School of Engineering and Management

Air Force Institute of Technology

Air University

Air Education and Training Command

In Partial Fulfillment of the Requirements for the

Degree of Master of Science in Aerospace Engineering

Paul B. Wilson, BS

Captain, USAF

March 2019

**DISTRIBUTION STATEMENT A.**
APPROVED FOR PUBLIC RELEASE; DISTRIBUTION UNLIMITED.

AFIT-ENY-MS-19-M-253

# TACTICAL MISSILE PERFORMANCE FOR SINGLE AND MULTI-WIRE EMBEDDED PROPELLANT CONFIGURATIONS WITH DISCONTINUITIES

Paul B. Wilson, BS

Captain, USAF

Committee Membership:

Dr. Carl R. Hartsfield, PhD
Chair

Lt Col M. Walker, PhD
Member

Maj D. Liu, PhD
Member

AFIT-ENY-MS-19-M-253

## Abstract

The overall intent of this research is to improve tactical missile range by increasing the total impulse through the addition of wires in solid propellant and to investigate performance impacts with discontinuities in the wire. The concept of wired end burners is to increase burning rates along the wire to develop larger burn areas which produce higher thrust over a shorter duration. For this research a model is developed to add wires, with or without discontinuities, to an end burner design and to provide performance results such as thrust, chamber pressure, mass flow, and impulse. This research compares a wireless baseline propellant to both single and multi-wire embedded configurations with varying materials and break locations. Five different wire materials are tested to investigate the performance for various thermal diffusivities and melting temperatures. The results for the wire material are also used to compare to previous research and validate the model developed. A theoretical carbon nanotube is included to demonstrate the impact of thermal diffusivity on burning rates and to provide evidence for future applications. Wire diameters are varied from 1-10 mm to find the optimal geometry for heat transfer into the propellant and nine evenly spaced locations for breaks along the wire are selected to investigate the impact a break has on total impulse. To ensure results are comparable, the geometry of the throat is adjusted for the various test runs to obtain missile performance at a typical operating chamber pressure near 4 MPa (580 psia). The analysis provided in this paper expands upon existing research by evaluating single- and multi-wire systems with small gaps in the wire. The results in this research show small gaps have negligible impact on performance and carbon nanotube fibers can theoretically provide up to 25% more total impulse than star and internal tube grains while still producing comparable thrust over similar action times.

# Acknowledgments

I would like to thank my thesis advisor, Dr. Hartsfield, for your guidance and support throughout this thesis effort. I appreciate your willingness to review my work and always making yourself available. Many thanks to Maj. Liu for serving on my committee, sponsoring this research, and allowing me the flexibility to pursue this topic. Thanks to Lt Col. Walker for serving on my committee. Finally, to my wife, thank you for supporting me through this process and keeping the family in order during these busy 18 months.

Paul B. Wilson

## Table of Contents

Page

## List of Figures

Page

# List of Tables

# TACTICAL MISSILE PERFORMANCE FOR SINGLE AND MULTI-WIRE EMBEDDED PROPELLANT CONFIGURATIONS WITH DISCONTINUITIES

## I. Introduction

### 1.1 General Issue

The need for greater standoff range in a hostile environment is ever present with the advancement of air defense capabilities. Improving the range of missiles will increase standoff distance for fighters and increase aircraft survivability. By demonstrating the capability of wired propellants, these configurations can be applied in two huge ways. First off, the solid rocket component of current inventory could be replaced with an improved design and secondly, future missiles systems can employ this technology to provide optimal desired performance. It is also important to ensure the reliability of these configurations as the potential for wire breaks during manufacturing has been observed.

### 1.2 Research Objectives/Hypotheses

While there is research into developing new solid propellant mixtures, this paper will focus on the addition of wires to known propellants to increase burning rate and improve total impulse. To evaluate the impact of embedded wires, as well as the operational impact of imperfect wires in a real inventory, this research sought to accomplish the following:

1. Create a model to analyze propellant burning characteristics with a single wire in an end burner configuration with or without a wire break.

2. Expand the model to include a variable number of wires and locations within the propellant.
3. Compare results to wireless designs with identical parameters.
4. Demonstrate performance improvements or deficiencies.

Based on previous experiments and models, it is expected the thrust will increase due to larger burn areas and increased mass generation. However, there is a finite amount of propellant and therefore the burn time is expected to decrease. This research will determine if these expected results increase or decrease total impulse and potential applications will be identified.

### 1.3 Assumptions/Limitations

For this research, dimensions will be estimated for a generic medium sized air-to-air missile and for propellant properties, values for the First-Stage Minuteman 1 Motor as presented in Sutton and Biblarz "Rocket Propulsion Elements," 9th edition, Table 12-1 are used [1]. The dimensions and propellant properties will remain constant for each test to ensure only wire effects are represented by the results. The flight profile is assumed straight and level and the ambient conditions at an altitude of 5.5 km are used to represent a realistic operating altitude for an air-to-air missile, however, several simulations are run at different altitudes to show how performance will vary.

Inside the chamber, several assumptions are used to simplify the model. The walls of the chamber are considered adiabatic with no heat loss through them. The wire is treated as adding negligible mass to the flow, and not participating in combustion. The temperature in the chamber is kept constant at the adiabatic flame temperature of the propellant and the products of combustion are considered homogeneous and gaseous. Flow is considered uniform and normal at every axial location from throat to exit to utilize ideal rocket equations.

Analysis for the multi-wire simulation is limited to predictions from the single-wire model. For example, if a seven-wire grain analysis is desired, the single-wire model is adjusted to account for the different diameter required to fit seven symmetrical tubes into one tube. The results of the single-wire model are then manipulated to represent the seven-wire model which will provide skewed results. Qualitatively, the results are beneficial for considering future possibilities and research, however, the quantitative results for multiwire grains, while indicative of trends, should not be used for design purposes.

## II. Literature Review

### 2.1 Overview

To achieve the research objectives laid out previously, a proper understanding of the fundamentals is necessary. This chapter covers the basics principles of rocket propulsion such as mechanics, thermodynamics, and chemistry [1]. Furthermore, solid propellant rocket motor principles will be studied to determine what parameters can be manipulated to increase performance. The three avenues of heat transfer: conduction, convention, and radiation are also examined to understand how heat from combustion is transferred throughout the wire and propellant. To model heat transfer, discretization methods are discussed to convert complex analytical equations into programmable equations which will accurately represent reality. Finally, previous research is summarized to provide background, justify assumptions, and validate results obtained.

### 2.2 Rocket Propulsion

#### 2.2.1 Rocket Fundamentals

For rockets, propulsion is achieved due to the momentum created by high velocity combustion products ejected out of the nozzle. The basis of the ideal rocket equation is Newton's 2nd law:

$$F = \frac{d}{dt}(mv) = m\frac{dv}{dt} + v\frac{dm}{dt} \tag{1}$$

where $F$ is the rate change of momentum and mass is assumed constant. This is can be manipulated to obtain the definition of momentum,

$$Fdt = mdv \tag{2}$$

or,

$$Impulse = Fdt \tag{3}$$

and by integrating over the entire time of force application,

$$I_t = \int_0^t Fdt \tag{4}$$

total impulse is found. Another well-known rocket performance metric is specific impulse, $I_s$ or $I_{sp}$, which represents the thrust per unit propellant “weight” flow rate [1]. Specific impulse can be represented in several ways,

$$I_s = \frac{\int_0^t Fdt}{g_0 \int_0^t \dot{m}dt} = \frac{I_t}{(g_0 m_p)} \tag{5}$$

where $g_0$ is standard Earth gravitational acceleration (9.8066 m/sec$^2$), $\dot{m}$ is propellant mass flow rate, and $m_p$ is the total amount of propellant expelled. Furthermore, the thrust can be derived by a summation of forces at the nozzle exit which produces, plus the momentum flux leaving the nozzle exit, producing Eq. 6 [1].

$$F = \dot{m}v_2 + (p_2 - p_3)A_2 \tag{6}$$

The exit velocity and mass flow rate are $v_2$ and $\dot{m}$, respectively, and together they represent the momentum thrust. The second term is the force the exit and ambient pressures exert at the nozzle exit area. With the goal of higher thrust in mind, nozzles are designed to cancel the pressure term or provide a slightly positive difference in most of their operating envelope [1]. Figure 1 depicts a general chamber and nozzle set up. To obtain the terms needed to solve for thrust, the ideal rocket equations described below can be used.

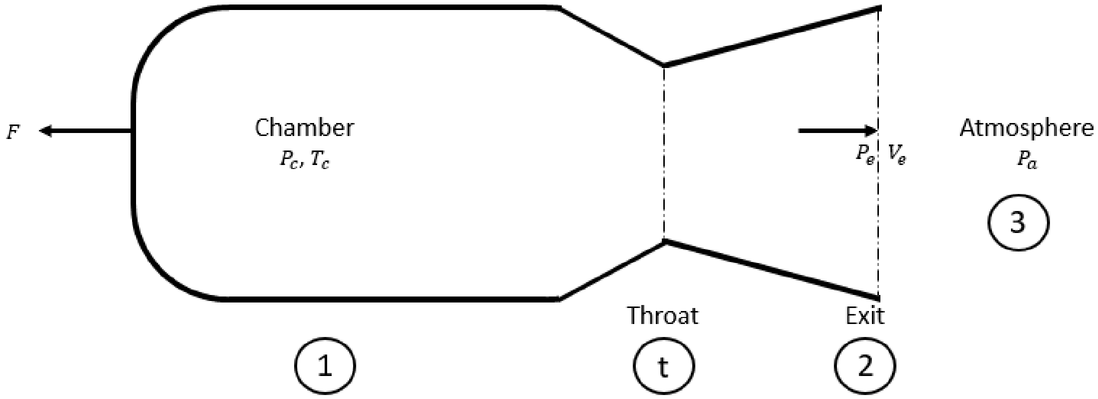

**Figure 1: Chamber and Nozzle**

### 2.2.2 Ideal Rocket Performance

Ideal rocket propulsion is defined using several assumptions which are also extended to this research. Combustion products are considered homogeneous, gaseous, and to obey the ideal gas law (Eq. 7), therefore, liquid or solid products are considered to be adding negligible mass to the flow.

$$p = \rho R T = \frac{mRT}{V} \tag{7}$$

Additionally, the chamber walls are treated as adiabatic with no heat transfer and wall boundary layer effects are neglected [1]. Finally, the flow is treated as uniform, continuous, and normal to the exit [1]. With the assumptions outlined, isentropic flow relations, nozzle theory, and continuity are used to derive the mass flow rate $\dot{m}$ and exit velocity $v_2$,

$$\dot{m} = A_t p_c \gamma \frac{\sqrt{[2/\gamma + 1]^{\gamma+1/\gamma-1}}}{\sqrt{\gamma R T_c}} \tag{8}$$

$$v_2 = \sqrt{\left(\frac{2\gamma}{\gamma - 1}\right) R T_c \left[1 - \left(\frac{p_2}{p_c}\right)^{\frac{\gamma-1}{\gamma}}\right]} \tag{9}$$

where,

$A_t$ = Throat Area (m²)
$p_c$ = Chamber Pressure (Pa)
$T_c$ = Chamber Temperature (K)
$\gamma$ = Ratio of Specific Heats for chamber mixture
$R$ = Gas Constant for the chamber mixture (J/kgK)

Substituting mass flow rate and exit velocity into Eq. 6 provides the ideal thrust equation,

$$F = A_t p_c \sqrt{\left(\frac{2\gamma^2}{\gamma - 1}\right)\left(\frac{2}{\gamma + 1}\right)^{\frac{\gamma+1}{\gamma-1}} R T_c \left[1 - \left(\frac{p_2}{p_c}\right)^{\frac{\gamma-1}{\gamma}}\right]} + (p_2 - p_3) A_2 \tag{10}$$

where,

$A_2$ = Nozzle Exit Area (m²)
$p_2$ = Exit Pressure (Pa)
$p_3$ = Ambient Pressure (Pa)

A relationship between exit area and throat area can be developed for supersonic nozzles from continuity where the mass flow at every location along the system is the same [1].

$$\frac{A_t}{A_2} = \left(\frac{\gamma + 1}{2}\right)^{1/\gamma - 1} \left(\frac{p_2}{p_c}\right)^{1/\gamma} \sqrt{\left(\frac{\gamma + 1}{\gamma - 1}\right)\left[1 - \left(\frac{p_2}{p_c}\right)^{\frac{\gamma-1}{\gamma}}\right]} \tag{11}$$

This relationship can be used to obtain nozzle and throat area dimensions to produce a desired pressure jump from chamber to the exit.

## 2.3 Solid Propellant Fundamentals

### 2.3.1 Grain Configuration

The selection of grain configuration is vital when designing a rocket motor due to the burn area relationship with mass flow and the volume of propellant able to be used. Figure 2 shows how different configurations provide different thrust profiles based on the evolution of the burn area.

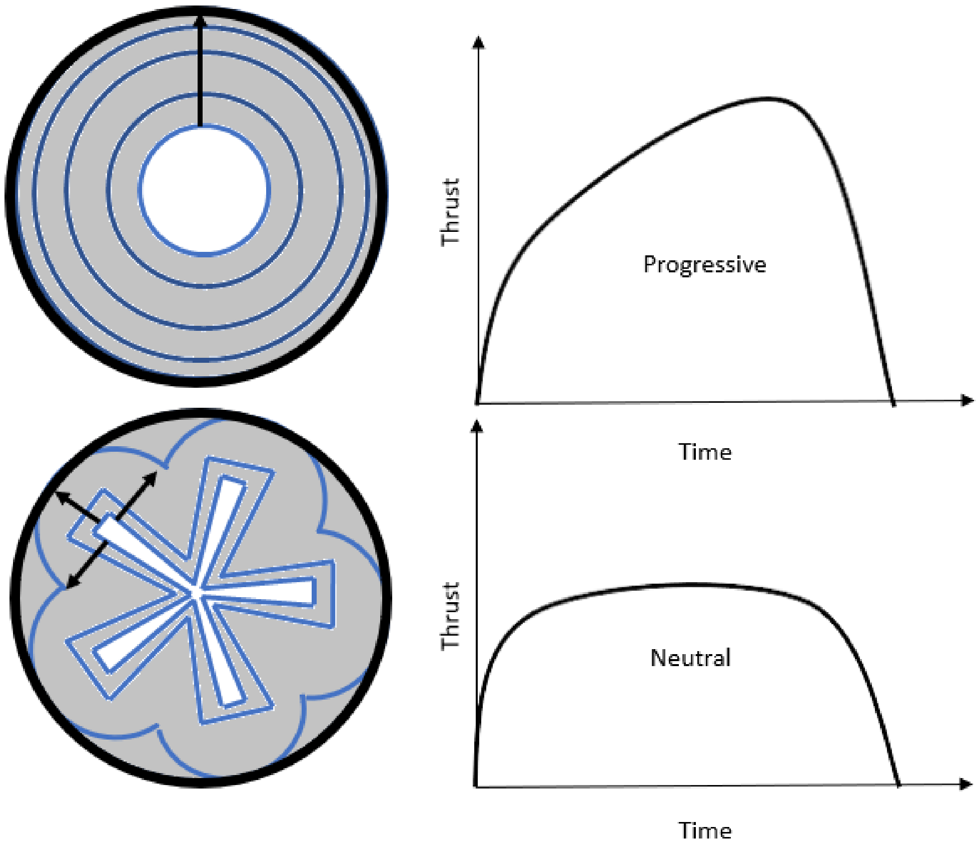

**Figure 2: Grain Configurations and Thrust Profiles.**

The end burner configuration, not shown above, is a solid cylinder of propellant which experiences burning only on the surface in contact with combustion and has the same burn area at every instant of time. It maximizes the amount of propellant which can be used and will also provide a neutral burn. A grain is classified as neutral, regressive, or progressive depending on if the pressure, thrust and burning surface are constant, decreasing, or increasing, respectively. The web fraction is defined as the ratio of the web thickness to the outer radius of the grain and is typically greater than one for end burners since the length of the propellant is considered the web thickness and for open internal configurations, the web fraction is less than one [1]. Volumetric fill fraction is the ratio of the volume of propellant to the volume of the chamber which is maximized (nearly 1) for end burners because there is no open space. Table 1 shows typical web fraction and volumetric fill fractions for different configurations [1].

**Table 1: Characteristics for several Grain Configurations, ref. Table 12-4 [1].**

| **Configuration** | **Web Fraction** | **Volumetric Fraction** | **Burning Characteristics** | **CG Shift** |
|---|---|---|---|---|
| **End Burner** | >1.0 | 0.9-0.98 | Neutral | Large |
| **Internal Burning Tube** | 0.5-0.9 | 0.8-0.95 | Neutral or Progressive | Small to moderate |
| **Internal Star** | 0.3-0.6 | 0.75-0.85 | Neutral | Small |
| **Wagon Wheel** | 0.2-0.3 | 0.55-0.70 | Neutral | Small |
| **Dendrite** | 0.1-0.2 | 0.55-0.7 | Neutral | Small |
| **Dog Bone** | 0.2-0.3 | 0.7-0.8 | Neutral | Small |

Of notable concern for the end burner is the center of gravity (CG) shift. Most of the burn area for the other configurations comes from the outboard burning due to the open internal area in contact with combustion, which means area is being lost axially at about the same rate. For end burners, the CG will shift forwards as propellant burns in one direction. Burn area will also be low compared to open configurations such as those mentioned above and will thus produce lower thrust. End burners are typically used for missions which require long burn times and low thrust [2]. Typical tactical motor configurations are star or some kind of slotted tube design which provide greater thrust over less time [3]. The goal of augmenting the end burner with highly conductive wire is to maximize volumetric fill fraction while increasing the burn area and burn rate to increase thrust.

For this research, pressure and thrust for each test run will be averaged over the thrust action time which is the burning time between the initial and final 10% thrust points on the thrust-time curve. Figure 3 shows what this action time looks like.

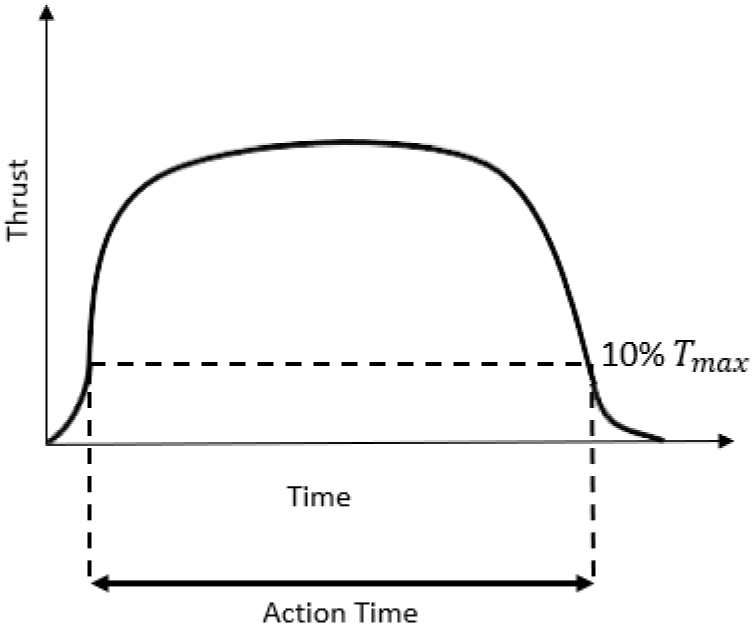

**Figure 3: Definition of Action Time.**

### 2.3.2 Burning Rate

The burning rate is an important factor for solid rockets because it correlates to mass flow rate and thrust. As burn rate increases, mass flow rate and thrust will increase, however, the propellant will be exhausted more rapidly. Therefore, it is essential to determine the right burn rate for the appropriate application. In all configurations, the grain burns normal to the surface.

The generation rate of product gas from solid propellant is given by [1]

$$\dot{m} = A_b r \rho_b \tag{12}$$

where,

$A_b$ = Burn Area (m²)
$r$ = Burn Rate of propellant (m/s)
$\rho_b$ = Solid Propellant Density (kg/m³)

From continuity, the mass flow rate generated must equal the sum of the mass storage per time in the chamber mass and the mass flow rate out of the nozzle [1]. Mathematically, this breaks down to:

$$A_b r \rho_b = \frac{d(\rho_c V_c)}{dt} + \frac{A_t p_c}{c^*} \tag{13}$$

where the subscript $c$ represents chamber values and $c^*$ is the characteristic velocity which is a non-physical parameter used to compare rocket performance. The storage term is usually neglected due to the small mass of gaseous propellant required to fill the added volume in comparison to the mass of solid propellant previously in the volume [1]. Now rearranging equation 13 provides a way to relate chamber pressure and the burn rate:

$$p_c = \frac{A_b r \rho_b c^*}{A_t} \tag{14}$$

Analytically, it is hard to predict the burning rate for different propellants, so the burning rate is normally empirically fit from experimental data at various conditions. For most propellants, the empirical equation is of the form:

$$r = a p_c^n \tag{15}$$

where $a$ and $n$ are propellant specific. The temperature coefficient, $a$, is an empirical constant which is dependent on the ambient grain temperature and has units based on the units of $r$ and $p_c$ [1]. The burning rate exponent or pressure exponent, $n$, is a dimensionless number and is strictly propellant dependent.

As mentioned above, the temperature coefficient is dependent on the grain temperature. This is an important term to discuss because the grain temperature will be impacted as the wire conducts heat into the propellant and increases the temperature. It should also be noted that at operational altitudes, temperatures for missiles vary significantly with temperatures experienced ranging from 219-344 K [1]. There are two terms used to characterize the burning rate sensitivity to temperature: the temperature sensitivity of burning rate, $\sigma_p$, or the temperature sensitivity of pressure, $\pi_p$.

$$\sigma_p = \left(\frac{\partial \ln r}{\partial T_b}\right)_{p_c} = \frac{1}{r}\left(\frac{\partial r}{\partial T_b}\right)_{p_c} \tag{16}$$

$$\pi_K = \left(\frac{\partial \ln p_c}{\partial T_b}\right)_{A_b/A_t} = \frac{1}{p_c}\left(\frac{\partial p_c}{\partial T_b}\right)_{A_b/A_t} \tag{17}$$

Both terms have units of per temperature and values of each are obtained from strand burner tests and small- or full-scale motor tests, respectively [1]. The relationship between $\sigma_p$ and $\pi_K$ is identified through integration and logarithmic calculations of the two previous equations. First, Eq. 15 is written in log-form [1]:

$$\ln r = \ln a + n \ln p_c \tag{18}$$

Now, plugging this term into the $\ln r$ term of equation 16 results in,

$$\sigma_p = \left(\frac{\partial(\ln a + n \ln p_c)}{\partial T_b}\right)_{p_c} = \left(\frac{\partial \ln a}{\partial T_b}\right)_{p_c} \tag{19}$$

And then distributing, integrating, and taking exponents on both sides produces

$$a = a_o e^{\sigma_p (T_b - T_{0b})} \tag{20}$$

where $T_b$ is the current grain temperature, $T_{0b}$ is the nominal grain temperature, and $a_o$ is a burn rate coefficient which does not depend on temperature. Knowing $a_o$ and $\sigma_p$ is valuable because it allows the temperature coefficient to be updated based on grain temperature variations, thus updating the burn rate. Conducting a similar procedure for equation 17 provides the relationship for the two sensitivity variables,

$$\sigma_p = (1 - n)\pi_K \tag{21}$$

With key variables identified and appropriate substitutions made, the relationship between the burning rate and the temperature coefficient is,

$$r = a_o e^{\sigma_p (T_b - T_{0b})} p_c^n \tag{22}$$

Equation 22 is the backbone of this study as it shows increasing the grain temperature $T_b$ will increase the burn rate which is the expected behavior along the wire.

### 2.3.3 Chemistry

The chemical makeup of a solid propellant is selected with a specific mission in mind. Whether it be for low signature (smokeless), specific performance, or storage stability the selection of ingredients is very important [4]. While it is not the purpose of this research to identify the best performing propellant in combination with wires, it is important to acknowledge different propellants will have different properties ($\rho$, $C_p$, $k$, $a$, $n$, etc.) and thus effect the heat conduction and burn rate in the propellant. According to Davenas, there are six families of propellants: Extruded Double-Base Propellants (EDB), Cast Double-Base Propellants (CDB), Composite Modified Cast Double-Base Propellants (CMDB), Elastomeric Modified Cast Double-Base Propellants (EMCDB), Composite Propellants, and High-Energy Propellants. EDB and CDB propellants primarily consist of nitrocellulose (NC) and nitroglycerine (NG) and are considered homogeneous since both oxidizer and fuel are part of the same molecules [3, 5]. The difference between the two are minor additives and the production process. CMDB and EMCDB propellants are derived from EDB and CDB propellants with the addition of RDX and/or HMX for improved density and performance. All four of these types are considered smokeless or minimum smoke based on only consisting of carbon, hydrogen, oxygen, and nitrogen molecules, with products consisting mostly of $CO_2$, $H_2O$, and $N_2$ [3]. For simplicity, these first four types of propellants can be considered double-base propellants. The last two propellant types can be combined into the composite propellant family due to their heterogeneous grain [1]. Both are designed with oxidizer crystals (typically Ammonium Perchlorate, AP) and powdered fuel (often Aluminum, Al) which are bound together with a (normally non-energetic) binder (usually polybutadiene, HTPB). The high energy propellants get their distinction for the addition of RDX or HMX to the propellant, as part of the binder mixture. A composite propellant is selected for this research and it is important to note the addition of aluminum powder into the propellant will increase the thermal conductivity and also classify it as a smoky propellant due to the oxidized aluminum particles in the exhaust.

The selection of wire material is also of high importance. More thermally conductive materials will result in increased heat penetration lengthwise into the propellant. Typically, silver, copper, aluminum, and tungsten wires are considered for their heat conductivity (and, at least for tungsten, high melting point) [3]. Additionally, the size of the wire will be an important design factor. Larger diameters will lead to greater heat flux into the wire but will also lead to more heat flux out of the wire due to the increase in contact surface area with the propellant. Also, increasing the size of the wire will decrease the volume of propellant. The effects of the wire size and material on rocket performance will be documented in the results.

For the purpose of this research, the wire and propellant are considered to always be in contact and to be completely parallel to the chamber walls with no curves which would produce uneven burning. However, it's important to note manufacturing wire-embedded propellants is a delicate task. In final form, after the propellant is cast around the wire, the wire must be rectilinear or burn back will be uneven [3]. Additionally, the thermal expansion coefficients for the wire and propellant are important. If they are significantly different, this may result in gaps between the wire and propellant as they expand and contract due to thermal cycling [3]. Thermal cycling is unavoidable due to the temperature changes with altitude experienced during aircraft operations.

## 2.4 Heat Transfer

### 2.4.1 First Law of Thermodynamics

Using the first law of thermodynamics and conservation of energy, a starting point for modeling heat transfer in the propellant and wire can be derived. The first law, depicted in Figure 4 and numerically in equation 23, states the total energy in a control volume must equal the amount which enters and is produced in the volume minus the amount that exits [6].

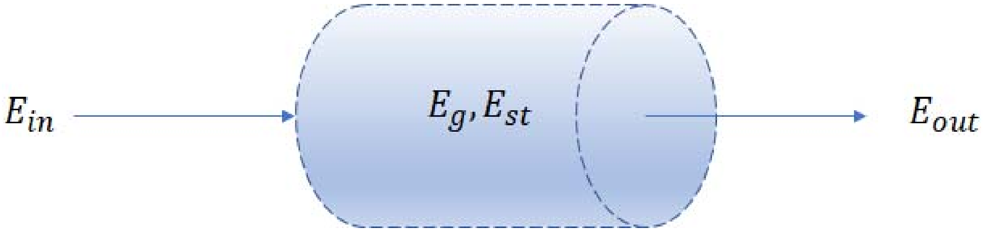

**Figure 4: Energy Balance for a Control Volume.**

$$E_{in} - E_{out} + E_{gen} = E_{st} \tag{23}$$

For this research, there is no energy generated within the solid propellant or wire so the energy balance used is,

$$E_{in} - E_{out} = E_{st} \tag{24}$$

The next three sections discuss the avenues for which heat is transferred and will provide terms to fit into the energy balance above.

### 2.4.2 Conduction

Heat transfer is the transit of thermal energy due to a temperature gradient [6]. Conduction is the transfer of heat between particles on a molecular level where there is no bulk motion occurring. Energy is transferred via translational motion of the molecules as well as internal rotational and vibrational modes [6]. There is no bulk motion in the propellant and wire so conduction will be the mode of transfer inside the system. Bearing in mind the design of the end burner with a wire inside, conduction will occur through the wire lengthwise as it is heated by the combustion gases and then conduction will occur from the wire to the surrounding propellant in contact and diffuse through the propellant radially.

This diffusion of energy is characterized by Fourier's law, or the rate equation, and is expressed as [6]

$$q''_{cond} = -k\frac{dT}{dx} \tag{25}$$

where $k$ (W/mK) is the thermal conductivity of a material, $q''$ is the heat flux (or heat flow per unit area), and $dT/dx$ is the temperature gradient in the material. This equation indicates more thermally conductive wires will result in a higher heat flux. Now considering a cylindrical control volume such as the one in Figure 5, an energy balance can be derived considering only conduction and energy storage.

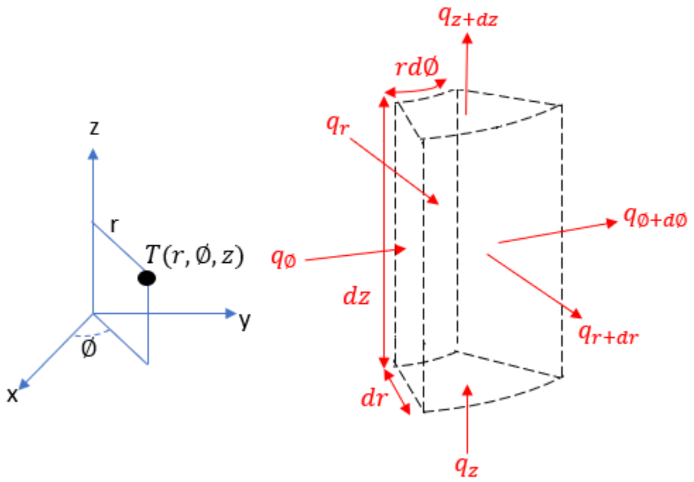

**Figure 5: Cylindrical Control Volume.**

This produces the cylindrical form of the heat diffusion equation shown below [6].

$$\frac{1}{r}\frac{\partial}{\partial r}\left(kr\frac{\partial T}{\partial r}\right)+\frac{1}{r^2}\frac{\partial}{\partial \emptyset}\left(k\frac{\partial T}{\partial \emptyset}\right)+\frac{\partial}{\partial z}\left(k\frac{\partial T}{\partial z}\right)= \rho C_p\frac{\partial T}{\partial t} \tag{26}$$

From symmetry of the wire and propellant, the flux in the Ø-direction is assumed to be zero and assuming the thermal conductivity is constant and isotropic gives

$$\frac{k}{r}\frac{\partial}{\partial r}\left(r\frac{\partial T}{\partial r}\right)+k\frac{\partial^2 T}{\partial z^2}= \rho C_p\frac{\partial T}{\partial t} \tag{27}$$

By isolating the time derivative, a common set of variables is identified and together are known as thermal diffusivity $\alpha$ (m²/sec).

$$\alpha = \frac{k}{\rho C_p} \tag{28}$$

Thermal diffusivity measures the ability of a material to conduct heat relative to its ability to store thermal energy [6]. The effect thermal diffusivity has on increased burning rate will be presented in the results. Through boundary conditions and discretization methods discussed later, equation 27 is modified to track the temperature profile for the interior portion of the propellant.

### 2.4.3 Convection

Whereas conduction does not encompass bulk fluid motion, convention does. The hot combustion gases in the chamber will transfer heat through convection to all surfaces in contact. The exposed propellant and the exposed end of the wire will receive this heat and diffuse it through conduction lengthwise. The rate equation for convection is known as Newton's law of cooling and is expressed as

$$q''_{cond} = h(T_s - T_\infty) \tag{29}$$

where $h$ (W/m²K) is the convection heat transfer coefficient which depends on conditions in the boundary layer [6]. There are many ways to determine the convection coefficient for laminar and turbulent flows which require geometric assumptions and the velocity profile near the surface. Previous work from Caveny, Glick, and King all use Navier-Stokes equations to solve for velocity near the wire-propellant intersection and determine a heat coefficient [7, 8]. They also assume radiation from combustion gas is small compared to convection and neglect it. Smith performed analytical predictions for experimental heat transfer coefficients at the nozzle for various chamber pressures [9]. His results for $h$ ranged from roughly 2000-4000 W/m²K for chamber pressures of 220, 410, and 742 psia. These results are used to justify the calculated convection coefficient used in the model for this research. Of note, Smith's results are calculated at the nozzle where velocity is greater than at the propellant interface. It is assumed the convection coefficient would be smaller at the propellant interface but still on the same order of magnitude. For this research, the heat convection is assumed constant and radiation is considered a factor. The technique used to find the convection coefficient for this research is detailed in chapter 3.

### 2.4.4 Radiation

Radiation is the transfer of energy through electromagnetic waves and does not require a medium, unlike conduction and convection [6]. While conduction and convection dominate the heat transfer environment in the motor, radiation is still present. Radiation is the main source of heat transfer for the wire break scenario where there is a physical gap at some location on the wire. Convection and conduction in the very small region of stagnant air between the wire ends are considered negligible. Radiation emitted from a perfectly emitting black body is

$$E_b = \sigma T_s^4 \tag{30}$$

where $\sigma$ is the Stephan-Boltzmann constant (5.67x10$^{-8}$ W/m$^2$K$^4$) and $T_s$ is the surface temperature [6]. The wires used are not blackbody so the actual radiation emitted is

$$E = \varepsilon \sigma T_s^4 \tag{31}$$

where $\varepsilon$ is the emissivity of the material. To determine the flux of energy into or out of an object, the difference between emitted and absorbed is determined and shown by

$$q''_{rad} = \varepsilon \sigma (T_s^4 - T_{sur}^4) \tag{32}$$

where $T_{sur}$ is the surrounding temperature or the other wire end in this case. This heat flux term is crucial to modeling the wire break situation and will also be used to approximate the convection coefficient. For this research, a view factor of one is considered for both the wire break and propellant interface. The gap between the wires is assumed to be small and therefore the radiation is only transferred from wire to wire and not to the propellant. At the surface, it is assumed the propellant only sees the combustion gases and therefore has a view factor of one.

## 2.5 Numerical Methods

### 2.5.1 Overview

Numerical methods are used to solve complicated partial differential equations (PDE) using finite difference approximations (FDA) or discretized forms of the PDE to simplify the mathematics. Complex calculus is converted to algebra, allowing the use of computers to solve the system of equations at a large number of discrete points. It is also an effective way to obtain sufficient or beneficial data which can reduce or eliminate the number of experiments or tests required.

Physical processes governed by PDEs can be classified into three categories: equilibrium, eigenvalue, or propagation problems [10]. This research falls under the propagation problem category due to the physical nature of the transient temperature distribution.

### 2.5.2 Finite Difference and Taylor Series Expansion

To create a finite difference method for a PDE, the definition of a derivative is examined. In equation 34 below, the derivative of temperature in the x-direction is broken down into the difference between temperatures at two points. As the distance between the two points goes to zero, the right-hand side (RHS) gets closer to the actual partial derivative at the location.

$$\frac{\partial T}{\partial x} = \lim_{\Delta x \to 0} \frac{T(x_0 + \Delta x, y_0) - T(x_0, y_0)}{\Delta x} \tag{33}$$

Since it is not practical or efficient to reduce the $\Delta x$ or grid spacing to zero, Taylor Series Expansions (Eq. 34) are performed to provide a finite-difference representation which includes truncation error (T.E.).

$$T(x_0 + \Delta x, y_0) = T(x_0, y_0) + \Delta x \frac{\partial T}{\partial x_{x_0,y_0}} + \frac{(\Delta x)^2}{2!} \frac{\partial^2 T}{\partial x^2{}_{x_0,y_0}} + \cdots + \frac{(\Delta x)^n}{(n)!} \frac{\partial^n T}{\partial x^n{}_{x_0,y_0}} \tag{34}$$

Rearranging the equation to isolate the first derivative yields equation 35 which is nearly identical to equation 34 but with T.E.

$$\frac{\partial T}{\partial x_{x_0,y_0}} = \frac{T(x_0+\Delta x,y_0)-T(x_0,y_0)}{\Delta x} \underbrace{- \frac{\Delta x}{2!} \frac{\partial^2 T}{\partial x^2{}_{x_0,y_0}} - \frac{(\Delta x)^2}{(n)!} \frac{\partial^n T}{\partial x^n{}_{x_0,y_0}}}_{TE} \tag{35}$$

The smaller the $\Delta x$ term becomes, the smaller the leading T.E. term will be thus making the overall approximation of the derivative more accurate. The above equation is called the forward difference because the $\Delta x$ is in the positive direction. The T.E. is first order, $O(\Delta x)$, for the forward difference and is commonly presented as,

$$\frac{\partial T}{\partial x_{x_0,y_0}} = \frac{T(x_0+\Delta x,y_0)-T(x_0,y_0)}{\Delta x} + O(\Delta x) \tag{36}$$

The same procedure shown above can be done using a $\Delta x$ in the negative direction to derive the backward difference.

$$T(x_0 - \Delta x, y_0) = T\left(x_{0,y_0}\right) - \Delta x \frac{\partial T}{\partial x_{x_0,y_0}} + \frac{(\Delta x)^2}{2!} \frac{\partial^2 T}{\partial x^2{}_{x_0,y_0}} - \cdots + \frac{(\Delta x)^n}{(n)!} \frac{\partial^n T}{\partial x^n{}_{x_0,y_0}} \tag{37}$$

Or,

$$\frac{\partial T}{\partial x_{x_0,y_0}} = \frac{T(x_0,y_0)-T(x_0-\Delta x,y_0)}{\Delta x} + O(\Delta x) \tag{38}$$

To obtain the central difference, Eq. 37 is subtracted from Eq. 34 which ends up cancelling the $\partial^2 T/\partial x^2$ term and leaving the leading T.E. term with a $(\Delta x)^2$.

$$\frac{\partial T}{\partial x_{x_0,y_0}} = \frac{T(x_0 + \Delta x, y_0) - T(x_0 - \Delta x, y_0)}{2\Delta x} + O[(\Delta x)^2] \tag{39}$$

Oppositely, adding Eq. 34 and Eq. 37 produces an approximation for the second derivative:

$$\frac{\partial^2 T}{\partial x^2}_{x_0,y_0} = \frac{T(x_0 + \Delta x, y_0) - 2T(x_0, y_0) + T(x_0 - \Delta x, y_0)}{(\Delta x)^2} + O[(\Delta x)^2] \tag{40}$$

The technique of adding Taylor Series can be utilized to represent a higher order derivative as well as the use of three or more points to improve accuracy. The first and second derivative approximations are all the only two needed to model the energy balance.

### 2.5.3 Explicit vs. Implicit

The difference between explicit and implicit methods comes down to the number of unknowns in the finite-difference equation. Explicit schemes have only one unknown which appears in the equation and can be solved in terms of known quantities [10]. Implicit schemes are comprised of several unknowns from the next time step which can be solved simultaneously from data already know. The positives of implicit schemes are they tend to be stable no matter what the time step or spatial step is selected (always stable for linear systems) and the computer processing is much quicker. The downside is they are much more complicated to solve for nonlinear problems where solving simultaneous equations is challenging. Explicit schemes are much easier to produce but take longer to process and solution stability becomes of great concern. An explicit approach is used in this research as the problem is explicitly transient with a number of significant non-linearities in properties and physics.

### 2.5.4 Stability

From section 2.5.3, stability is identified as an important factor for marching problems [10]. If the truncation error is increasing over time, the approximate solution is getting further from the actual value. Taking a closer look at an example discretized form of one-dimensional transient heat conduction,

$$T_{i,j}^{p+1} = Fo_z(T_{i,j+1}^{p} - 2T_{i,j}^{p} + T_{i,j-1}^{p}) + T_{i,j}^{p} \tag{41}$$

a term called the Fourier Number is produced where

$$Fo_z = \frac{k\Delta t}{\rho C_p \Delta z^2} = \frac{\alpha \Delta t}{\Delta z^2} \tag{42}$$

where all the terms are constant. Analyzing equation 41 reveals the Fourier Number is the controlling factor for stability for explicit schemes. With thermal diffusivity already known from the propellant, the time and spatial step have the only influence on stability. If the Fourier number is too small, the equation will take forever to reach the actual solution. And if it is too large, the value at the next time step will continue to grow and eventually become unstable. This can all be imagined as applying a linear estimate to a parabolic function. Over small increments, the errors are small and projecting forward does not result in large problems, but pushing too far results in large errors and these are multiplicative in the growth of the solution state. In systems with any oscillatory behavior possible, this results in positive feedback to the oscillatory behavior and non-physical outputs, such as negative temperatures (on an absolute scale).

For linear PDEs, Lax's Equivalence Theorem holds true that convergence can be proven for a well-posed initial value problem if the FDA satisfies the consistency condition and is stable [10, 11]. Consistency is shown by subtracting the PDE from the

FDE and taking the limit as the mesh spacing goes to zero [10]. If the limit is zero, the FDE is consistent with the PDE. Stability is proven by showing error from any source is not permitted to grow over time. In general, stability criteria can be solved for using the Von Neumann Analysis. This becomes increasingly challenging as the number or terms and the order of the PDE increases. A more simplistic approach but potentially more time intensive process is guess and check. The time step and spatial step can be estimated and tweaked based on the results achieved. This is verified by time step independence testing where smaller timesteps are shown to not change the answer.

## 2.6 Relevant Research

### 2.6.1 Early Testing

The first known testing of modified propellant with embedded wires was performed in the 1950's. Testing at the Naval Ordnance Test Station (NOTS) in 1953 by McEwan et al. involved the addition of short metal wires scattered throughout the propellant with varying size and composition [12]. Around the same time in 1954, the Atlantic Research Corporation were testing propellants with single, long wires of varying size and composition as well as different coatings on the wires [13, 14, 15]. In 1982, Kubota et al. conducted experiments on double-base propellants with various wire materials in an end burner configuration [16]. The propellants were chosen for their translucent qualities so the flame and temperature profile could be tracked visually. Figure 6 represents results from Kubota at 0.8 sec and 1.2 sec after ignition for an 8 mm diameter silver wire. It is from these experiments which Caveny and Glick and King were able to analytically model the results. To date, the biggest success of wired propellants has come from surface-to-air applications. Both the shoulder-launched Redeye and its successor, the Stinger, employ wired end burners [17].

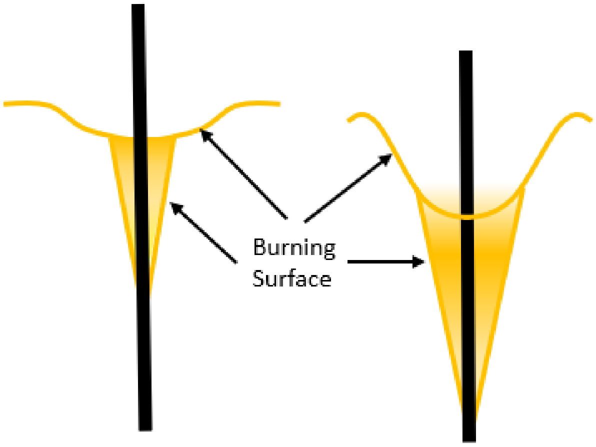

**Figure 6: Cone Shape Burning Surface after 0.8s and 1.2s after Ignition [16].**

### 2.6.2 Caveny and Glick

In 1967, Caveny and Glick developed the first model to account for transient and steady burning along metal fibers [7]. They investigated the burning along a single rectangular, nonreactive, metal fiber and broke it into three phases [7]. Phase one consists of the increase in burning along the wire compared to a no wire condition. This is followed by the steady-state segment where the burning area is constant. Lastly, there is an increase in burning rate as the burning surface reaches the end of the wire [7]. They broke down the typical conical shape of the burning surface into several regions shown in Figure 7. The fiber thermal zone is the area which experiences a temperature increase from the fiber. The interaction zone temperature is related to conduction from the wire and combustion gas from the chamber. The propellant burning surface zone is very thin as most propellants are good insulators. Finally, the gas phase reaction layer is where most of the chemical reactions take place [7]. The thicknesses of the fiber thermal and interaction zone are a few millimeters and the fiber thermal zone is roughly a centimeter or two long depending on the wire and propellant properties [7].

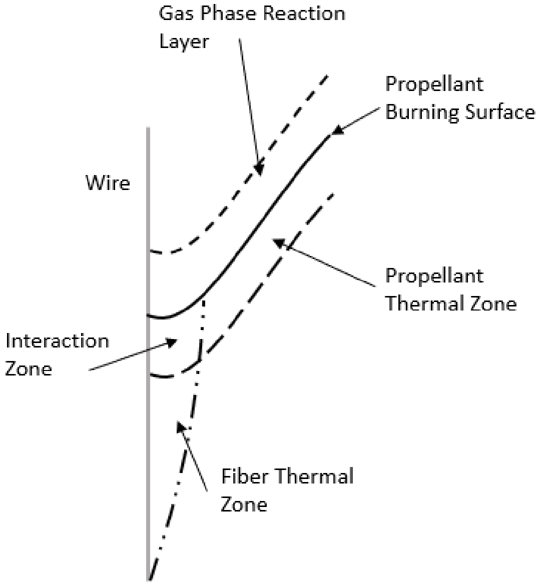

**Figure 7: Regions created from burning around the Fiber [7].**

They assumed heat transfer from the fiber to the interaction zone could be neglected in comparison to the fiber in the thermal zone and heat conduction parallel to the fiber could be neglected in comparison to the heat conduction perpendicular to the fiber [7]. Effects of the gas-phase reaction zone are negligible and flow in the cone is quasi-steady, incompressible, and inviscid except at the fiber [7]. The fiber is rectangular in cross section and is thermally thin [7]. Lastly, the propellant is isotropic and all properties are constant and the temperature distribution in is two-dimensional [7].

From the assumptions above, the Caveny-Glick model is developed. Conduction along the fiber reduces to [7]

$$\left(\rho C_p\right)_f \left(\frac{\partial T_f}{\partial t}\right) = k_f \left(\frac{\partial^2 T_f}{\partial z^2}\right) + \frac{pq''}{A_f} \tag{43}$$

where $\rho$ is the density of the fiber, $C_p$ is the specific heat capacity of the fiber, $T_f$ is the temperature of the fiber, $k_f$ is the thermal conductivity of the fiber, $p$ and $A_f$ are the perimeter and cross-sectional area of the fiber, and $q''$ is the heat flux into the wire. The heat flux for exposed wire ($e$) and for the wire beneath the surface in contact with the propellant ($p$) are given as [7]:

$$q'' = q_e'' = h\left(T_g - T_f\right) + \sigma F\left(T_g^4 - T_f^4\right) \tag{44}$$

$$q'' = q_p'' = k_f\left(\frac{\partial T_p(0,z,t)}{\partial x}\right) \tag{45}$$

One area of concern is when the fiber starts to melt. The boundary condition will change depending on the melting temperature of the fiber compared to the propellant flame temperature. If the fiber melts before the propellant does, the boundary will be constrained to the melting temperature of the fiber and will move as the fiber burns. This new phase boundary becomes [7],

$$A_f k_f \frac{\partial T_f(z_m,t)}{\partial x} + A_f \rho_f L_f s = A_m q_e''(z_m,t) \tag{46}$$

where the subscript $m$ represents the melted fiber, $L_f$ is the latent heat of fusion for the fiber, and $s$ is the melting rate of the fiber. For the scenario when the fiber melting temperature is greater than the propellant flame temperature, the exposed wire heat flux is simply,

$$q_e''(0,t) = k_f\left(\frac{\partial T_p(0,t)}{\partial z}\right) \tag{47}$$

until the melting temperature is reached.

To determine the heat transfer from the fiber into the propellant, Caveny and Click started with the one-dimensional, transient energy equation

$$\frac{\partial T_p}{\partial t} = \alpha_p \left( \frac{\partial^2 T_p}{\partial z^2} \right) \tag{48}$$

using the temperature boundary conditions in the x-direction for the grain edge and fiber and a uniform initial temperature throughout the propellant.

$$T_p(\infty, z, t) = T_i \tag{49}$$

$$T_p(0, z, t) = T_f \tag{50}$$

$$T_p(x, z, 0) = T_i \tag{51}$$

As mentioned above, the heat flux into the propellant beneath the burning surface $q_p''$ is required to solve for the temperature distribution at every location. Caveny and Glick employed Goodman's heat balance integral which approximates the heat flux into the propellant as [7, 17],

$$q_p''(z,t) = \frac{2{k_p}^2 \left[T_p(0,z,t) - T_i\right]^2}{3\alpha_p \int_0^t q_p''(z,\lambda) d\lambda} \tag{52}$$

They then adapted this equation to produce a numerical solution by expanding the integral in the denominator and solving for the local heat flux [7],

$$q_p''(z,t) = \frac{1}{2\Delta t} \left\{ \left[ Q_n^2(t) + \frac{8k_p^2}{3\alpha_p} \left[T_f(z_n, t+\Delta t) - T_i\right]^2 \Delta t \right]^{1/2} - Q_n(t) \right\} \tag{53}$$

by defining the variable $Q_n$ as,

$$Q_n(t+\Delta t) \cong Q_n(t) + q_p''(z_n, t+\Delta t)\Delta t \tag{54}$$

Now the local heat flux from the fiber to the propellant is obtained and only one additional node is needed [7].

The next challenge is obtaining the convective heat transfer coefficient for the exposed boundary of the wire. Using the geometry from Figure 7, Caveny and Glick formed equations for the radial and tangential velocity components for the combustion gases near the surface.

$$u = v_s \sin(\theta_c - \theta) \tag{55}$$

$$w = v_s \cos(\theta_c - \theta) \tag{56}$$

Using the cylindrical form of the Navier-Stokes equation, they were able to derive relationships between the cone angle and velocity. While assuming the fiber temperature doesn't vary much with distance and the exposed portion of fiber is very short and the Reynolds number will be small, Caveny and Glick determined the convection coefficient could be calculated using laminar flat plate equations [7]. They did note for certain angles of interest, heat transfer into the fiber could increase by 40% to those obtained through flat plate calculations based on the higher mixing and turbulence experienced.

The results obtained from Caveny and Glick's model tend to support the experimental results from the McEwan et al. which showed thermal diffusivity, melting point, and radius of the wire were contributing factors to burning rate [12]. Table 2 shows the burning rates along the wires achieved for six different materials. The results show silver and tungsten are the best performers, silver being good for its thermal conductivity and tungsten for its high melting temperature.

**Table 2: Burn Rates Achieved using different Wire Materials [7].**

| Material | Thermal Diffusivity of fiber (in²/sec) | Average Burn Rate along fiber (in/sec) | Steady State Burn rate along fiber (in/sec) |
|---|---|---|---|
| **Copper** | 0.112 | 6.57 | 12.5 |
| **Aluminum** | 0.0904 | 4.55 | 5.2 |
| **Magnesium** | 0.0895 | 4.59 | 5.05 |
| **Tungsten** | 0.077 | 9.05 | 15.5 |
| **Steel** | 0.0109 | - | 2.6 |
| **Silver** | 0.192 | 7.6 | 16 |

Using a commercially available aluminum fiber, they tested for optimal fiber cross-sectional area and found 0.2x10$^{-5}$ in$^2$ (or 1.29x10$^{-3}$ mm$^2$ circular area equivalent) produced the best steady-state burn rate. For small rectangular fibers, Caveny and Glick determined the best performing wire materials and the optimal cross-sectional area.

### 2.6.3 King

King created an analytical model of effects of wires on solid motor ballistics which match closely with experimental data obtained in the 1950's. In Figure 8 below, he presents a diagram of heat flow in the area of concern based on historical data and assumptions made for the model.

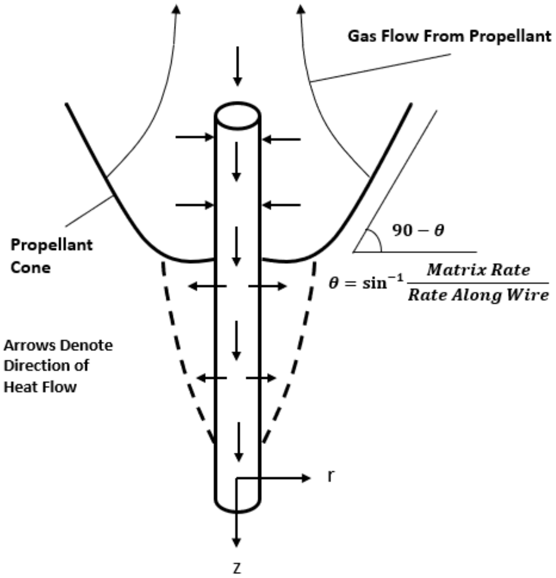

**Figure 8: King's Depiction of the Propellant-Wire Interaction Region [8].**

There are 8 major assumptions and approximations he uses to developed the model [8]:

1) Heat conduction is neglected in the propellant parallel to the wire.
2) Wire is isothermal radially.

3) Gas-phase reactions effects are neglected in the heat balance in the near wire region.
4) Radiation is neglected between wire and combustion flow.
5) Constant and isotropic propellant properties.
6) Wire properties are constant.
7) Wire that reaches melting temperature disappears.
8) A unique relationship between burn rate along wire and a mean temperature is assumed.

These assumptions are key to simplifying the mathematics and most are used in the model created for this research.

To create his model, King first illustrates the issue of calculating burn rates using temperatures outside which are used to find temperature sensitivity $\sigma_p$ for propellants. He relates temperature and burn rate at three points to form a polynomial fit so as to provide a basis for calculating burn rates at high temperatures. King also performs a mean temperature calculation at the interface between the wire and propellant to account for propellant thickness proportional to the characteristic matrix thermal-profile thickness [8].

King approaches the problem similar to Caveny and Glick by setting up the energy balance for each area of concern. The balance along the wire is set to be

$$\rho_w C_{p,w} \frac{\partial T}{\partial t} = k_w \frac{\partial^2 T}{\partial z^2} + \frac{4}{D_w} q'' \tag{57}$$

where the only difference between the models is the geometry of the wire used. By assuming radiation is ignored, the heat flux into the exposed wire is given as

$$q'' = h_{contact}(T_{prop,interface} - T_w) \tag{58}$$

Heat flux for the submerged section of wire in contact with propellant is

$$q'' = k_{prop} \frac{\partial T_{prop(r_{wire},t)}}{\partial r} \tag{59}$$

In the propellant, temperature gradients parallel to the wire are neglected which produces an energy balance of

$$\frac{\partial (rT)}{\partial t} = \alpha_{prop} \frac{\partial}{\partial r}\left(r \frac{\partial T}{\partial r}\right) \tag{60}$$

King then transforms equation 61 using the Lardner and Pohle integral method of analysis in cylindrical coordinates to express the temperature at any time and axial location as [18]

$$\tilde{T} = T - T_{bulk} = \frac{\left(q'' \frac{r_w}{k_{prop}}\right)\left(\eta - \frac{r}{r_{wire}}\right)^2 \ln\left(\frac{r}{r_{wire}\eta}\right)}{(\eta - 1)(2\ln\eta + \eta - 1)} \tag{61}$$

where $\delta$(z,t) is the thermal-wave thickness and $\eta$ is

$$\eta(z,t) = \frac{(\delta(z,t) + r_{wire})}{r_{wire}} \tag{62}$$

Lastly the temperature profile is substituted into equation 61 and integrated to solve for the heat flux and thermal profile at a given time.

His model found the optimal diameter for the types of wires he tested is around 3-4 mils or 0.07-0.1 mm at a chamber pressure of 1000 psia. All wires exhibited similar burn rate enhancement near the wire but the best results were achieved with silver. Comparing his data to the experimental data from ARC, his model tends to overpredict or underpredict the burn rate depending on the autoignition temperature selected for fitting a new burn rate. For an autoignition temperature of 550 K, his model overpredicts the burn rate over the entire pressure range of 200-2000 psi. For autoignition temperatures of 600 and 620 K, his model underpredicts from 200-600 psi and overpredicts from 600-2000 psi but is overall more accurate than the previous temperature of 550 K. Finally, he examined the effect of gaps between the wire and propellant and was able to show larger gaps reduce the heat transfer to the propellant and thus reduce the burn rate along the wire. Using a thermal conductivity of 0.042 W/mK for the gap, he showed a 0.1-micron gap had little effect on the burn rate but gaps larger than 1 micron started to show burn rate reduction on the order of 10% to 80% for a 33-micron gap. It should be noted for all gaps tested, the burn rate near the wire was still higher than the burn rate for just the propellant.

# III. Methodology

## 3.1 Overview

With the research objects defined above, the methods used for selecting material and filling in unavailable properties is discussed first, followed by the numerical method process, and then the MATLAB code implementation is detailed to describe how the simulation works.

## 3.2 Dimensions

The dimensions used for this research are estimated from 2012 weapon file data for an AIM-120C [19]. Figure 9 is a scaled version of the missile and it is through this image, estimates for the propellant, throat, and exit dimensions are obtained and shown in Table 3.

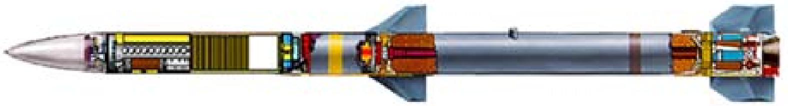

**Figure 9: AIM-120C Internal View [19].**

**Table 3: Approximate Geometry for AIM-120C.**

| Dimension | Diameter (m) | Cross-Section Area ($m^2$) | Length (m) | Volume ($m^3$) |
|---|---|---|---|---|
| **Missile** | 0.18 | 0.03 | 3.66 | - |
| **Propellant** | 0.16 | 0.02 | 0.6 | 0.012 |
| **Chamber** | 0.16 | - | 0.1 | 7.21E-4 |
| **Throat** | 0.0113-0.0451 | 9.98E-5-0.0016 | - | - |
| **Exit** | 0.0183-0.0734 | 0.0011-0.0169 | - | - |

The most contentious estimate is of the propellant length. From the image it looks like the propellant is roughly 40% of the entire length. Instead of using 40% of the missile for the length, the length is set to 60 cm's to achieve an L/D of 3.75 and reduce the duration of each simulation. This length is kept constant for each test iteration and thus the final length chosen is not of huge significance. The diameters for the propellant and nozzle are again estimated from the image and are determined to be slightly less than the diameter of the missile. For this research, the diameters are set to be the same. The throat diameter could also be estimated in a similar fashion but is instead found by substituting the mass flow rate generated from the propellant into the ideal rocket equation.

$$A_t = \frac{A_b r p_b}{p_c} \frac{\sqrt{RT_{comb}}}{\sqrt{\gamma[2/\gamma + 1]^{\gamma+1/\gamma-1}}} \tag{63}$$

Another geometry of concern is the initial volume of the chamber. It is assumed the initial shape of the chamber is similar to Figure 10,

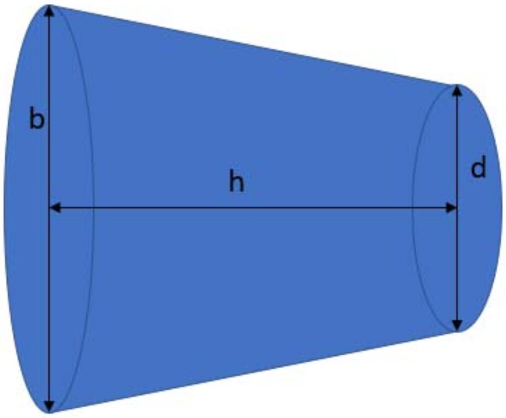

**Figure 10: Initial Volume of Chamber.**

where the larger diameter $b$ is located at the surface of the propellent, $d$ is the diameter of the throat, and $h$ is the estimated distance between the two diameters. The equation for volume is [20],

$$V = \frac{\pi h}{12}(d^2 + db + b^2) \tag{64}$$

The initial volume is vital because it is used in the ideal gas equation to find the initial mass in the chamber, and is part of the chamber volume calculation used to determine chamber pressure during the simulation.

## 3.3 Discretization Method

The key to accurately depict burn rates in the propellant is to track the temperature as the heat from combustion conducts into the wire and propellant. To accomplish this, an Explicit Forward Time Centered (FTCS) method is used knowing it is a propagation problem and initial and boundary conditions are known [10]. Energy balances are set up for all conditions encountered in the burn process. For reference, the origin of the system is the wire end in contact with the chamber, therefore this point is ($i$ =1, $j$ =1) for the matrix. The radial direction is represented by $i$, the axial direction or z-direction is represented by $j$, and the current time step is represented by $p$ . The full three-dimensional volume is accounted for by considering each node as a circular volume with some $\Delta r$ and$\Delta z$.

### 3.3.1 Convection Boundary

Initially, the convection boundary is only applied to the propellant surface open to combustion and the energy balance for nodes on the boundary is derived below starting with

$$E_{st} = E_{in} - E_{out} \tag{65}$$

and then breaking down the RHS with flux in and out of each surface of the node,

$$\rho C_p V\left(\frac{T_{i,j}^{p+1}-T_{i,j}^{p}}{\Delta t}\right) = hA\left(T_c - T_{i,j}^{p}\right) + kA\left(\frac{T_{i-1,j}^{p}-T_{i,j}^{p}}{\Delta r}\right) - kA\left(\frac{T_{i,j}^{p}-T_{i,j+1}^{p}}{\Delta z}\right) - kA\left(\frac{T_{i,j}^{p}-T_{i+1,j}^{p}}{\Delta r}\right) \tag{66}$$

where $V$ is the volume of the node and $A$ is the area of each surface. The first two terms on the RHS represent the flux into the node and the last two terms represent the flux out. The volume for each boundary node is

$$V = \pi\left[\left(r(i) + \frac{\Delta r}{2}\right)^2 - \left(r(i) + \frac{\Delta r}{2}\right)^2\right]\frac{\Delta z}{2} \tag{67}$$

where $r$ is the radial location of each node and the $\Delta z$ is halved to account for being on the boundary. The three surface area equations encountered are shown below,

$$A = 2\pi\left[r(i) - \frac{\Delta r}{2}\right]\frac{\Delta z}{2} \tag{68}$$

$$A = 2\pi\left[r(i) + \frac{\Delta r}{2}\right]\frac{\Delta z}{2} \tag{69}$$

$$A = \pi\left[\left(r(i) + \frac{\Delta r}{2}\right)^2 - \left(r(i) + \frac{\Delta r}{2}\right)^2\right] \tag{70}$$

where the first equation is the wire side radial surface area, the second is the outer radial surface area, and the third is the front and back axial area which is the same for both $\Delta z$ directions. Substituting in these variables and isolating the temperature at the new time gives the final equation for the convection boundary.

$$T_{i,j}^{p+1} = \frac{2h\Delta t}{\rho_p C_{p_p}\Delta z}\left(T_c - T_{i,j}^{p}\right) + \frac{2\alpha_p \Delta t\left[r(i)-\frac{\Delta r}{2}\right]}{\Delta r\left[\left(r(i)+\frac{\Delta r}{2}\right)^2-\left(r(i)+\frac{\Delta r}{2}\right)^2\right]}\left(T_{i-1,j}^{p} - T_{i,j}^{p}\right) - \frac{2\alpha_p \Delta t\left[r(i)+\frac{\Delta r}{2}\right]}{\Delta r\left[\left(r(i)+\frac{\Delta r}{2}\right)^2-\left(r(i)+\frac{\Delta r}{2}\right)^2\right]}\left(T_{i,j}^{p} - T_{i+1,j}^{p}\right) - 2Fo_{z_p}\left(T_{i,j}^{p} - T_{i,j+1}^{p}\right) \tag{71}$$

This boundary condition is only valid when there is convection on one side and conduction on the other three. When the conical burn profile starts to develop, the inside radial surface becomes open to the chamber and the discretization becomes

$$T_{i,j}^{p+1} = \frac{h\Delta t}{\rho_p c_{p_p} \Delta z}\left(T_c - T_{i,j}^p\right) + \frac{h\Delta t\left[r(i)-\frac{\Delta r}{2}\right]}{\rho_p c_{p_p} \Delta r\left[\left(r(i)+\frac{\Delta r}{2}\right)^2-\left(r(i)-\frac{\Delta r}{2}\right)^2\right]}\left(T_{i-1,j}^p - T_{i,j}^p\right) - \frac{\alpha_p \Delta t\left[r(i)+\frac{\Delta r}{2}\right]}{\Delta r\left[\left(r(i)+\frac{\Delta r}{2}\right)^2-\left(r(i)-\frac{\Delta r}{2}\right)^2\right]}\left(T_{i,j}^p - T_{i+1,j}^p\right) - Fo_{z_p}\left(T_{i,j}^p - T_{i,j+1}^p\right) \tag{72}$$

The 2 drops off from each term since the boundary will only exist inside the matrix where the volume of a node is related to $\Delta z$ not $\Delta z/2$. Figure 11 illustrates the two boundary conditions mentioned above.

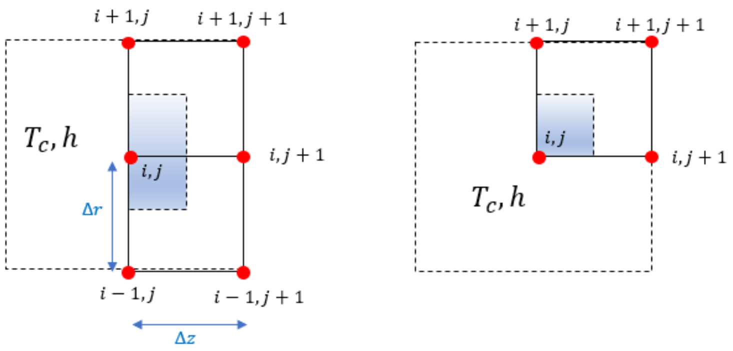

**Figure 11: Convection Boundary Conditions.**

### 3.3.2 Wire

The wire is assumed to be isothermal radially due to the high conductivity and the relatively low diameter compared to the length of the wire. For this reason, the wire is treated as one node at every axial location and makes up the lower boundary of the system. The volume of each wire node is accounted for to ensure the heat flux is captured accurately. Similar to equation 71, the initial convection boundary is

$$T_{i,j}^{p+1} = \frac{2h\Delta t}{\rho_w c_{p_w} \Delta z}\left(T_c - T_{i,j}^{p}\right) - \frac{2k_p \Delta t}{\rho_w c_{p_w} r_w \Delta r}\left(T_{i,j}^{p} - T_{i+1,j}^{p}\right) - 2Fo_{z_w}\left(T_{i,j}^{p} - T_{i,j+1}^{p}\right) \qquad (73)$$

where the middle term represents heat loss into the propellant which is why the thermal conductivity of the propellant is used and the last term is the energy loss into the wire axially. As the propellant adjacent to the wire starts to be consumed, the radial surface area of the wire becomes exposed and the flux is no longer conduction into the propellant but is now convection into the wire. The energy balance now becomes,

$$T_{i,j}^{p+1} = \frac{h\Delta t}{\rho_w c_{p_w} \Delta z}\left(T_c - T_{i,j}^{p}\right) + \frac{h\Delta t}{\rho_w c_{p_w} r_w \Delta r}\left(T_{i,j}^{p} - T_{i+1,j}^{p}\right) - Fo_{z_w}\left(T_{i,j}^{p} - T_{i,j+1}^{p}\right) \qquad (74)$$

where the 2 is dropped again to consider the full volume of the wire (there will be moments in the simulation where the first node experiences this condition and the 2 is accounting for). For the situation where the wire is exposed radially to convection but not cross sectionally, the equation becomes:

$$T_{i,j}^{p+1} = \frac{h\Delta t}{\rho_w c_{p_w} r_w \Delta r}\left(T_{i,j}^{p} - T_{i+1,j}^{p}\right) + Fo_{z_w}\left(T_{i,j-1}^{p} - 2T_{i,j}^{p} + T_{i,j+1}^{p}\right) \qquad (75)$$

where the second term is the combined heat conduction in and out of the node. The final scenario encountered by the wire is when it is fully submerged in the propellant where only conduction is a factor.

$$T_{i,j}^{p+1} = Fo_{z_w}\left(T_{i,j-1}^{p} - 2T_{i,j}^{p} + T_{i,j+1}^{p}\right) - \frac{2k_p \Delta t}{\rho_w c_{p_w} r_w \Delta r}\left(T_{i,j}^{p} - T_{i+1,j}^{p}\right) \qquad (76)$$

### 3.3.3 Wall Boundaries

The boundary between the propellant and the missile make up two of the four boundaries for this system. Assuming the walls are adiabatic, or perfect insulators, the heat flux out of those nodes is zero. Simply put, the conduction and convection condition will change as the node on the wall is exposed to the chamber but will always have no heat flux out. The volume and surface area for these boundaries are adjusted to account for only having either half the $\Delta r$ or $\Delta z$ depending on the wall.

### 3.3.4 Interior Propellant

The only form of heat transfer experienced inside the propellant is conduction. The discretized energy balance for the interior propellant nodes is,

$$T_{i,j}^{p+1} = \frac{\alpha_p \Delta t\left[r(i)-\frac{\Delta r}{2}\right]}{\Delta r\left[\left(r(i)+\frac{\Delta r}{2}\right)^2-\left(r(i)-\frac{\Delta r}{2}\right)^2\right]}\left(T_{i-1,j}^{p} - T_{i,j}^{p}\right) - \frac{\alpha_p \Delta t\left[r(i)+\frac{\Delta r}{2}\right]}{\Delta r\left[\left(r(i)+\frac{\Delta r}{2}\right)^2-\left(r(i)-\frac{\Delta r}{2}\right)^2\right]}\left(T_{i,j}^{p} - T_{i+1,j}^{p}\right) + Fo_{z_p}\left(T_{i,j-1}^{p} - 2T_{i,j}^{p} + T_{i,j+1}^{p}\right) \tag{77}$$

where the first two terms are radial heat condition in and out of a node and the last term is the heat conduction in and out in the axial direction. To account for the row of propellant nodes in contact with the wire, the radial conduction term into the node now uses the thermal conductivity and temperature of the wire

$$T_{i,j}^{p+1} = \frac{k_w \Delta t r_w}{\rho_p C_{p_p} \Delta r\left[\left(r(i)+\frac{\Delta r}{2}\right)^2-{r_w}^2\right]}\left(T_{i-1,j}^{p} - T_{i,j}^{p}\right) - \frac{\alpha_p \Delta t\left[r(i)+\frac{\Delta r}{2}\right]}{\Delta r\left[\left(r(i)+\frac{\Delta r}{2}\right)^2-{r_w}^2\right]}\left(T_{i,j}^{p} - T_{i+1,j}^{p}\right) + Fo_{z_p}\left(T_{i,j-1}^{p} - 2T_{i,j}^{p} + T_{i,j+1}^{p}\right) \tag{78}$$

which will sufficiently depict the heat transfer from the wire to the propellant.

## 3.4 MATLAB Implementation

### 3.4.1 Overview

For overview, the main function code is set to initialize the nodal structure as well as the properties of the propellant, chamber, and ambient conditions. With these items set, the data is run through a loop where temperature and mass of the propellant is updated at each time step and is then used to update the chamber conditions and performance of the missile. Figure 12 provides a description of what the code is doing.

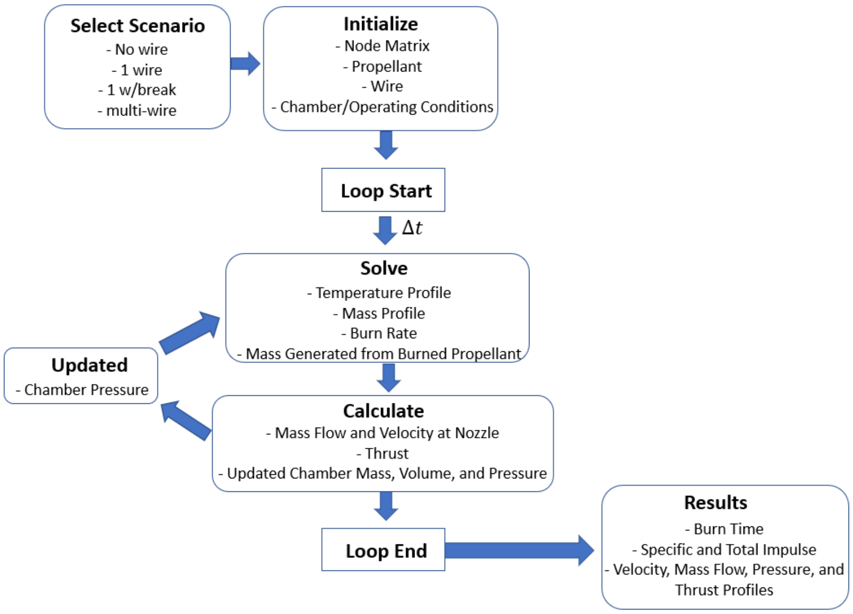

**Figure 12: Flow Chart for MATLAB code.**

### 3.4.2 Initialization

The propellant selected for this research is a composite propellant consisting of 70% ammonium perchlorate ($NH_4ClO_4$), 16% aluminum (Al), and 14% binder which is the same propellant used for the First-Stage Minuteman 1 Missile motor [1]. Table 4 provides the properties of the propellant implemented in the code. The specific heat capacity for the mixture is not available so a $C_p$ is calculated using

$$C_p = \frac{\sum_{j=1}^{m} n_j C_{p_j}}{\sum_{j=1}^{m} n_j} \tag{79}$$

where $n_j$ is the molar concentration of species $j$ and $C_{p_j}$ is the specific heat for species $j$.

**Table 4: Properties for First-Stage Minuteman 1 Missile [1].**

| **Property** | **Propellant** |
|---|---|
| **Composition** | 70% $NH_4ClO_4$,16% Al,14% Binders |
| **Density, $\rho$ (kg/m³)** | 1,760.44 |
| **Thermal Conductivity, $k$ (W/mK)** | 0.502 |
| **Molar Mass, $M$ (kg/mol)** | 29.30 |
| **Gas Constant, $R$ (J/kgK)** | 283.77 |
| **Specific Heat Capacity, $C_p$ (J/kgK)** | 1,551 |
| **Burning Rate, $r$ (mm/s) @ 6.8947 MPa** | 8.86 |
| **Burning Rate Exponent, $n$** | 0.21 |
| **Temperature Coefficient (m/sPa$^n$)** | 3.21E-4 |
| **Adiabatic Flame Temperature (K)** | 3,472 |

From Cai *et al.*, the $C_p$ for AP and Hydroxyl-terminated polybutadiene (HTPB) is 1460 J/kgK and 2860 J/kgK [21]. HTPB is assumed to be the 14 % of binder. From Sutton, the $C_p$ of crystalline Al is 807 J/kgK [1]. Using these values in equation 80 gives the mixture a combined $C_p$ of 1551 J/kgK. The thermal conductivity is also not readily available for the Minuteman 1 composition but a value of 0.502 W/mK is obtained from the work of Buckmaster *et al.* [22]. Their work is centered around modeling composite propellants burning with ultrafine aluminum particles in AP and binder. The thermal conductivities they use for calculating the combined thermal conductivity of the mixture are 0.405 W/mK for AP, 204.1 W/mK for Al, and 0.276 W/mK for the binder.

The burning rate provided is only valid at 1000 psi. To account for the variation in burning rate due to temperature and pressure, the temperature coefficient $a_o$ is solved for with the parameters from Table 4 where $T_b$ is 294 K and $T_{ob}$ is 288 K for the burn rate given.

$$a = a_o e^{\sigma_p (T_b - T_{ob})} = \frac{r}{p_c^n} \tag{80}$$

This gives a temperature coefficient $a$ of $3.2477x10^{-4}$ (m/sPa$^n$) and $a_o$ of $3.212x10^{-4}$ (m/sPa$^n$). Considering the average operating pressure to be 4 MPa or 580 psia, a new burn rate is calculated to be 0.0073 m/s. Although it may not be completely representative for an air-to-air tactical missile, its properties were readily available and the overall selection of propellant is trivial as it is kept the same for each run. Results will vary by changing the propellant but it is not in the scope of this research to study propellant effects.

The wire properties are initialized by selecting one of the six materials listed in Table 5. Additionally, the diameters of the wires will vary from 1 to 10 mm to determine the significance of wire diameter on burn rate enhancement near the propellant.

**Table 5: Properties of Wire Material [6].**

| Material | Density (kg/m$^3$) | Thermal Conductivity (W/mK) | Specific Heat Capacity (J/kgK) | Thermal Diffusivity (m$^2$/s) | Emissivity | Melting Temperature (K) |
|---|---|---|---|---|---|---|
| **Multi-Wall Carbon Nanotube** [23, 24] | 1,300 | 3,000 | 740 | 3.12E-3 | 0.98 | 2,600 |
| **Silver, polished** | 10,500 | 429 | 235 | 1.74E-4 | 0.02 | 1,235 |
| **Copper, polished** | 8,933 | 401 | 385 | 1.17E-4 | 0.03 | 1,358 |
| **Aluminum, polished** | 2,702 | 237 | 903 | 9.71E-5 | 0.04 | 933 |
| **Tungsten, polished** | 19,300 | 174 | 132 | 6.83E-5 | 0.04 | 3,660 |

With dimensions for the missile already known, the nodal matrix is determined by choosing a desired spatial step in the r- and z-direction. In the discretization equations provided in section 3.2, notice there is a $\Delta t/\Delta r^2$, $\Delta t/\Delta z^2$, $\Delta t/\Delta z,$ or $\Delta t/\Delta r$ constant in front of each term. To achieve stability, a trial and error approach is used to determine the time step and spatial step. An appropriate axial step $\Delta z$ is found to be 1 mm, the radial step $\Delta r$ is set to 0.5 mm, and the time step $\Delta t$ is set to 1 msec. The time step is modified to 0.1 msec while conducting simulations with CNT since the thermal conductivity is roughly 10 times larger. As discussed earlier, it is the relative magnitude of the Fourier number which matters. If the spatial step is reduced, the time step must decrease appropriately as to not exceed this stable magnitude. If all three are reduced ($\Delta z$, $\Delta r$, $\Delta t$) simultaneously, accuracy can be improved because the solution is becoming more consistent with the physics, however, this will increase the computational time of the code greatly.

With the matrix set, temperature and mass at each node is initialized. For temperature, each node is set to the desired ambient temperature. Due to the symmetry of the propellant grain, mass is initialized to account for the full three-dimensional volume for the two-dimensional matrix. With the density of propellant already known, equation 81 is used to set the mass accordingly at each node.

$$m(i,j) = \rho V = \rho[\pi\left(r_{i+\frac{\Delta r}{2}}^2 - r_{i-\frac{\Delta r}{2}}^2\right)dz] \tag{81}$$

The chamber values also require initialization to properly track the performance. The chamber pressure is set to a desired operating condition, the temperature is set to the adiabatic flame temperature for the propellant, and the volume of the open chamber is found from equation 65. The ideal gas law is then used to find the mass in the chamber which will fluctuate as the propellant is consumed and as the mass flow out of the nozzle changes.

$$m_c = \frac{p_c V_c}{R T_c} \tag{82}$$

An equivalence method is used to calculate the convection coefficient $h$. It is assumed to be constant and is found by setting convection in the chamber equal to radiation from combustion products, which gives equation 83:

$$hA\left(T_c - T_p\right) = \varepsilon\sigma A(T_c^4 - T_p^4) \tag{83}$$

and hence,

$$h = \varepsilon\sigma(T_c^2 + T_p^2)(T_c + T_p) \tag{84}$$

where $\varepsilon$ is the emissivity of the chamber gas mixture, $T_c$ is the chamber temperature, and $T_p$ is the initial temperature of the propellant. The emissivity is approximated to be 0.8 based on results from Dombrovsky who found the emissivity of optically thick clouds of alumina particles for temperatures of 3400 K and 3600 K were between 0.75-0.814 and 0.806-0.861 for varying sizes of the particles [25]. Also, the radiation is largely Short to Mid-Wavelength infrared, where most things have relatively high absorptivity or emissivity. This gives a convection coefficient $h$ of 2047 $(W/m^2K)$ which is on the low end for what Smith found for a nozzle [9]. It is determined this calculated value for $h$ is sufficiently representative of actual convection in a solid rocket chamber even though the approximation is crude.

### 3.4.3 Temperature and Mass Profile

During the simulation, combustion temperature is held constant and is used for all nodes which portray the convection boundary condition. Additionally, as the mass of each node becomes zero, the new temperature of said node becomes the combustion temperature. Elsewise the temperature of each node is consistent with the initial ambient temperature plus the changes from the discretized equations up to the current time step.

The relationship between temperature and mass is directly related. As the temperature of the propellant increases, the burn rate will increase and the propellant will be consumed faster. To account for this change, a new burn rate is calculated at each time step for each cell exposed to burning. The burn distance can then be found by multiplying the burn rate by the time step. To account for the situation when a node has two faces open to the chamber, an additional burn rate and burn distance is calculated in the radial direction. With these burn distances, a percentage of mass from each boundary node is lost which is in turn used to update the new chamber and performance values. When the burn distance becomes larger than the $\Delta z$ or $\Delta r$ for a node, the mass of said node becomes zero and the temperature of the node is now the combustion temperature. Since the burn distance will most likely never land on exactly the $\Delta z$ or $\Delta r$ location, the code is designed to consume mass from the next node for burn distances overlapping a border.

The wire is treated as having negligible impact to the chamber conditions and is therefore only treated as a boundary condition for the propellant. As the wire reaches its melting point, it falls off and adds no mass to the chamber fluid. The mass of the wire is still tracked for each time step because the heat flux into the wire will change based on the amount of wire exposed to the chamber.

### 3.4.4 Chamber/Exit Conditions

As the main performance metrics for missiles are specific impulse or total impulse, the thrust profile must be determined. To accomplish this, mass flow and exit velocity are calculated from updated chamber and exit pressures. At each time step, a new chamber pressure is calculated using ideal gas law with updated values of mass and volume in the chamber. Volume is found by dividing the density of propellant by the mass generated plus the previous volume. Chamber mass is updated with the new mass generated minus the mass flow out. With the chamber pressure now known, the constant pressure ratio $P_2/P_c$ can be applied to find the exit pressure. Also, this new chamber pressure is used to calculate the new burn rate for the next time step. Equation 10 can now be used to solve for thrust. After the thrust profile is created, thrust can be numerically integrated to solve for $I_t$,

$$I_t = \sum_{k=0}^{t} F_k \Delta t \tag{85}$$

and $I_{sp}$ is found using,

$$I_{sp} = \frac{I_t}{m_p g_o} \tag{86}$$

where $m_p$ is the total mass of the propellant and $g_o$ is the sea level acceleration due to gravity. With performance accounted for, results are tabulated graphically to compare the different scenarios.

### 3.4.5 Multi-Wire

The multi-wire arrangement is treated as an extension of the single-wire configuration due to the complex geometry observed in Figure 13. As the code is only designed for cylindrical propellants, there are empty gaps between the individual tubes as they are fitted inside the missile case.

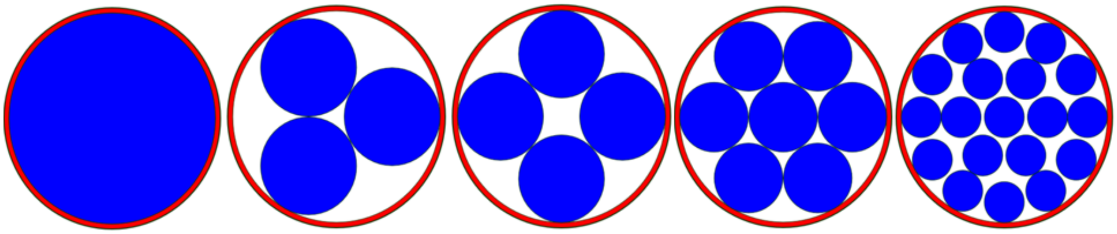

**Figure 13: Single vs Multiwire Cross-Sections.**

To account for this empty space, or the white area in Figure 13, the mass generated from the "empty" volume is found by using estimated burn area and burn rate term in equation 87,

$$m_{empty} = \rho_p A r_{ave} \Delta t \tag{87}$$

where,

$m_{empty}$ = Mass generated by "empty" volume (kg)
$A$ = Burn Area for "empty" volume (m²)
$p_p$ = Density of Propellant (kg/m³)
$r_{ave}$ = Average Burn Rate for "empty" volume (m/s)
$\Delta t$ = Time step (s)

Initially, the burn area for the "empty" volume is treated as an end burner until the first outer node of the individual tube experiences radially burning. Once this occurs, an estimated burn area is obtained from the cone angle created. The estimated steady state burn area will be different for each wire material due to the varying burn rates along the wire which produce cones with different angles. This estimation will not completely capture the complex geometry which occurs in the "empty" volume when the burn areas from the individual tubes are propagated out. The burn rate is found by taking the magnitude of the average radial and axial burn rates of a boundary node. For example, for the propellant mentioned earlier, each boundary node will experience burn rates of ~7-11.2 mm/sec as the node heats up and mass is still present. Therefore, the average burn rate is 9.1 mm/sec in both the radial and axial directions since the same conditions are used to solve for each. The specific values will change based on the propellant used but the process will stay the same. This will overestimate the burn rate during the progressive burning region when not all the surface area is exposed in the radial and axial directions but should be accurate for any surface exposed on both sides. The results for specific and total impulse are used to help establish this technique as it is expected the impulses would be approximately the same for each multiwire configuration since the mass of the propellant is relatively equal.

For the multiwire arrangements tested in this research, using the same chamber dimensions as before, the diameter of each individual tube is adjusted according. Table 6 shows the difference in grain composition for each scenario.

**Table 6: Mass and Fill Fraction for each Configuration.**

| Configuration | Volumetric Fill Fraction | Propellant Mass (kg) | Wire Mass (kg) |
|---|---|---|---|
| **No Wire** | 1 | 21.2374 | 0 |
| **1 Wire (2 mm Dia.)** | 0.9998 | 21.2341 | 0.0199 |
| **3 Wire (2 mm Dia.)** | 0.9995 | 21.2275 | 0.0594 |
| **4 Wire (2 mm Dia.)** | 0.9994 | 21.2242 | 0.0792 |
| **7 Wire (2 mm Dia.)** | 0.9989 | 21.2142 | 0.139 |
| **19 Wire (2 mm Dia.)** | 0.997 | 21.1744 | 0.376 |

To measure the effects of a discontinuity in one of the wires, both the single-wire break and no break simulations are run with the updated dimensions of the smaller tube. To keep the chamber calculations representative of a multiwire configuration, the mass generated for an individual tube is multiplied by the number of wires to represent each tube's contribution. This mass generated term plus the mass generated from the "empty" volume are used for calculating the chamber and nozzle performance at each time step. The final results for the break and no break mockups are then combined with proper weighting applied depending on the number of wires broken. For example, for a 7-wire configuration with one wire broken, the final results for exit velocity, mass flow, pressure, and thrust are weighted as followed: 85.71% for the no break results and 14.29% for the break results which accounts for production from six healthy wires and one broken wire. Additionally, the unburned propellant mass is tracked and an analysis of a potential center of mass shift is discussed in Section 4.7.

### 3.4.6 Internal Tube and Star

The internal tube and star configuration are used for further comparison. The internal tube diagram is show in Figure 14 and the dimensions used for the inner diameter is 2 cm. The diagram for a 5-point star is shown in Figure 15 and the web fraction used is 0.36. The area in red represents the unburned slivers remaining after the web is fully burned out and conditions for useful thrust are no longer met. The selected dimensions provide the fill fractions and masses shown in Table 7.

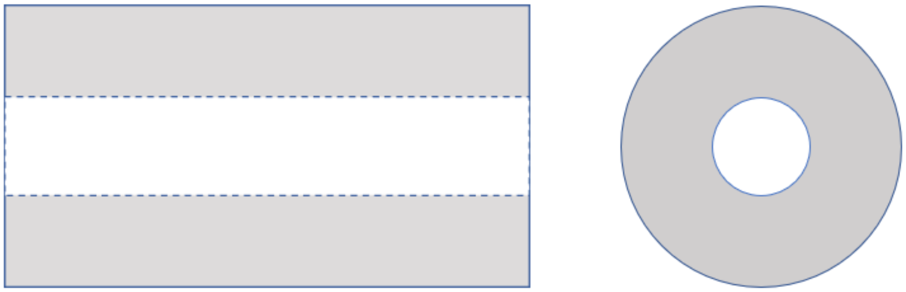

**Figure 14: Internal Tube Side and Cross Section View.**

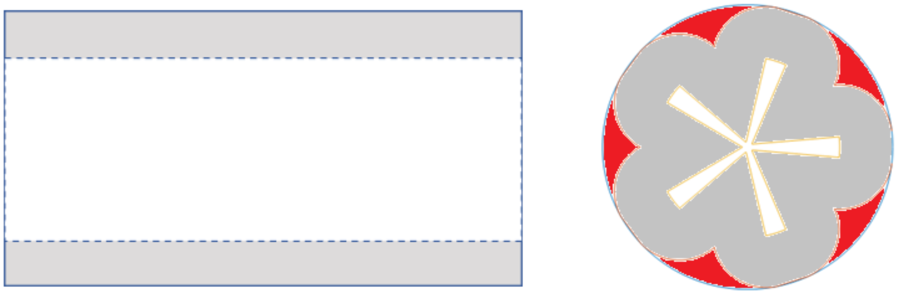

**Figure 15: 5-Point Star Side and Cross Section View.**

**Table 7: Fill Fraction and Propellant Mass for Internal Tube and Star Configuration.**

| Configuration | Volumetric Fill Fraction (Useful) | Propellant Mass (kg) | Sliver Mass (kg) |
|---|---|---|---|
| **Internal Tube** | 0.9375 | 19.9101 | 0 |
| **5-point Star** | 0.9026 (0.7886) | 19.1679 | 2.6334 |

Instead of discretizing the heat flux equations and creating a matrix for the propellant, the burning area is tracked over time and the mass generated at each time step is calculated. The same chamber initialization is conducted as before except now the initial volume includes the open internal volume. The mass generated at each time is then run through the same chamber and nozzle code as before to find the new chamber pressure and thrust at each time step. For the internal tube, original MATLAB code was generated but for the star grain, existing MATLAB code was adapted to meet the requirements of this research.

### 3.5 Summary

The research goals are achieved through proper selection of propellant and missile dimensions, accurate discretization of the heat balance at every location, and correct implementation of the physics in MATLAB. Careful observations are required to ensure the results are comparable, and if not, adjusted and explained appropriately. See Appendix for complete details of the MATLAB code used.

# IV. Analysis and Results

## 4.1 Overview

This chapter will discuss the results of wire-embedded configurations compared to the wireless end burner, internal tube, and star configurations. First, the method for smoothing out fluctuations in the data is covered. A visualization of the burning process is provided and the results are presented for the different wire types and sizes, break location effects, and the multi-wire scenario.

## 4.2 Data Smoothing

The need for a smoothing process is identified as the chamber values fluctuate initially. This comes from the nature of the problem where boundary nodes heat up and burn rate increases meaning mass generation will fluctuate as this process repeats for the new boundary nodes. The fluctuations are also a product of the nodal surface geometry which consists of tiny cubes of mass instead of a smooth continuous surface. Decreasing the magnitude of the Fourier number will produce smaller fluctuations, however, computational time will increase. Instead, to achieve smooth curves, pressure and thrust are averaged every 250-time steps for the metallic wires and every 2500-time steps for CNT which equates to 0.25 sec intervals. Figure 16 compares the averaged and raw thrust data for a single-wire example. This graphic is typical for all wired simulations with the lines matching up very well which is validated by the small errors shown between the data sets in Table 8. The percent error is calculated using equation 88 for impulse, pressure, and thrust.

$$\% \, Error = \frac{|Ave - Raw|}{Raw} \, x \, 100 \qquad (88)$$

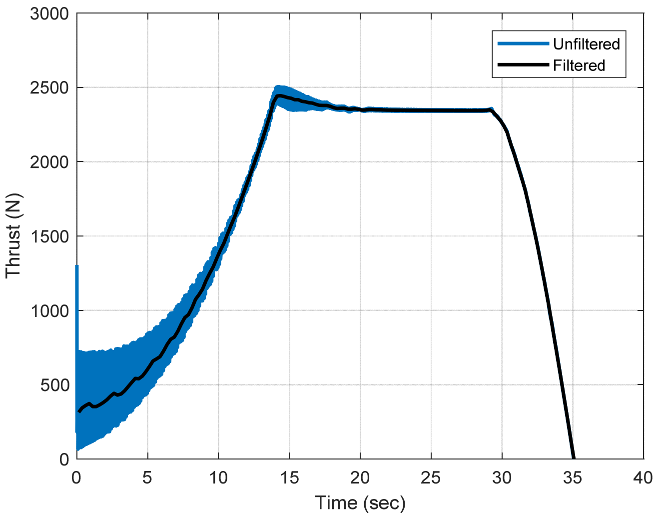

**Figure 16: Averaged vs Raw Data.**

**Table 8: Percent Error between Averaged and Raw data.**

| | **Averaged** | **Raw** | **Error (%)** |
|---|---|---|---|
| **Total Impulse ($10^4$ N*s)** | 5.880 | 5.881 | 0.015 |
| **Ave. Pressure (MPa)** | 4.528 | 4.530 | 0.033 |
| **Ave. Thrust ($10^3$ N)** | 1.692 | 1.689 | 0.177 |
| **Max Pressure (MPa)** | 6.066 | 5.962 | 1.714 |
| **Max Thrust ($10^3$ N)** | 2.504 | 2.443 | 2.424 |

The greatest error, relative to the others, is the calculation for max pressure and thrust and by looking at Figure 16, the peaks from the raw data are smoothed out by the averaging process. Overall, however, the process is shown to induce little error into the performance calculations. All data featured below in the results are treated with this smoothing process.

### 4.3 Wire Burn Visualization

To better understand the physical nature of the heat transfer and burning process, visual depictions of each are provided in this section. The evolution of the burning surface for a single wire configuration is shown in Figure 17 where the yellow area is the chamber mixture at 3,472 K and the blue area is the propellant at its ambient temperature of 252 K. Using this large scale, there is no noticeable temperature profile within the propellant due to its low thermal conductivity. A closer look at the propellant near the wire is required to capture the scale of heat transfer.

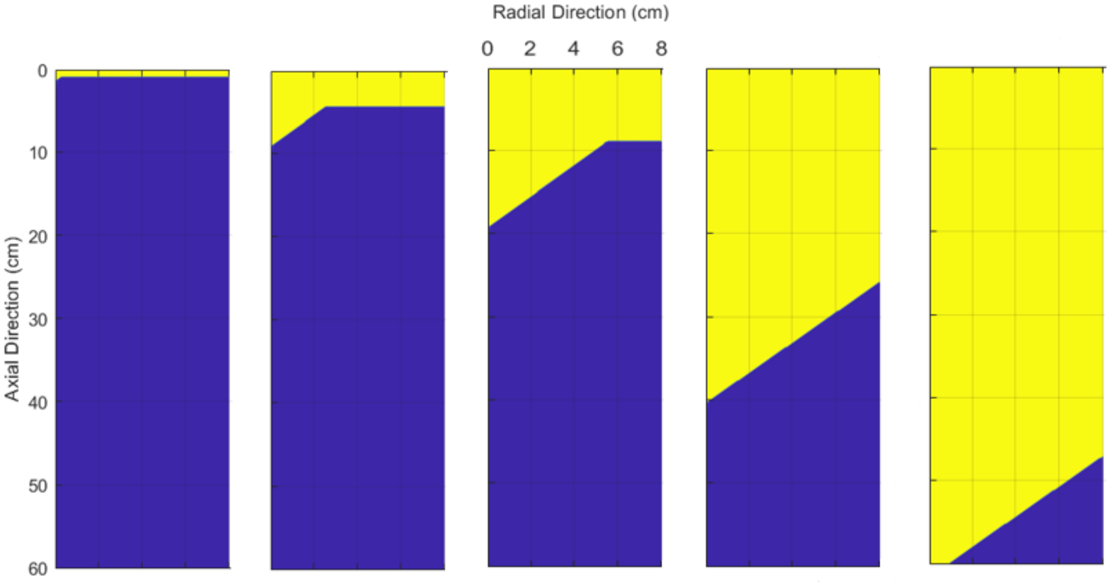

**a) 1 sec b) 5 sec c) 10 sec d) 20 sec e) 30 sec**

**Figure 17: Timeline of Burn Back for a Wire-Embedded Configuration.**

The timeline depicts progressive burning in Fig. 17 (a-c) where the surface area is increasing until it meets the wall, neutral burning in Fig. 17 (d) with the cone shape fully developed and unchanging, and a regressive burn in 17 (e) where the area is decreasing until burning is complete. This surface area development is directly correlated to the thrust and pressure profiles seen throughout the results.

To analyze the heat transfer from the wire to the propellant, the volume around the wire is magnified to see the temperature gradients. Figure 18 (a) depicts the steady-state burning interaction along the wire and shows the heat penetration to be 2 mm radially and 3 cm axially which aligns perfectly with Caveny and Glick's analysis of the thickness of the fiber thermal and interaction zone as being a few millimeters thick and the fiber thermal zone being a centimeter or two long depending on the wire and propellant properties [7]. When looking at the profiles with an appropriate scale, the profiles match up very well with the theoretical burn profiles shown in Figures 6-8 with silver producing a cone angle of 62 deg and CNT producing an angle of 82 deg.

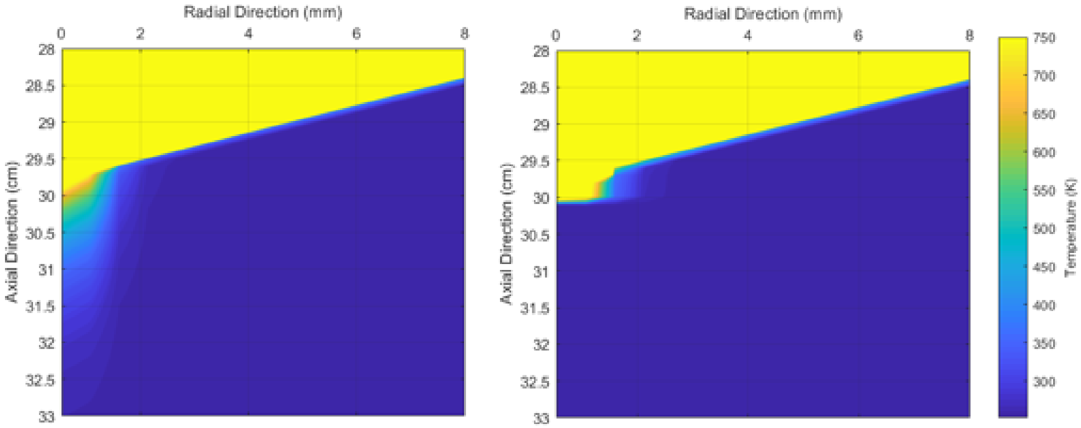

**a) No Break** **b) Break at 30 cm**

**Figure 18: Wire-Propellant Interaction Zone after 15 sec.**

In Figure 18 (b), heat transfer effects of a wire break can be clearly visualized. With only heat flux from radiation, the transfer of heat across the gap is shown to be insignificant. Once the wire becomes exposed to convection in the chamber, it starts to display the expected temperature profile. Figure 19 compares the two situations one second later. The temperature profile in the break scenario has already started to return to the steady state condition and is roughly 5 mm behind in burn location along the wire compared to the continuous wire. Looking at the overall burn area from 16-30 seconds for a break at 30 cm, Figure 20 shows the overall shape is only slightly affected compared to the burn area shown in Figure 17.

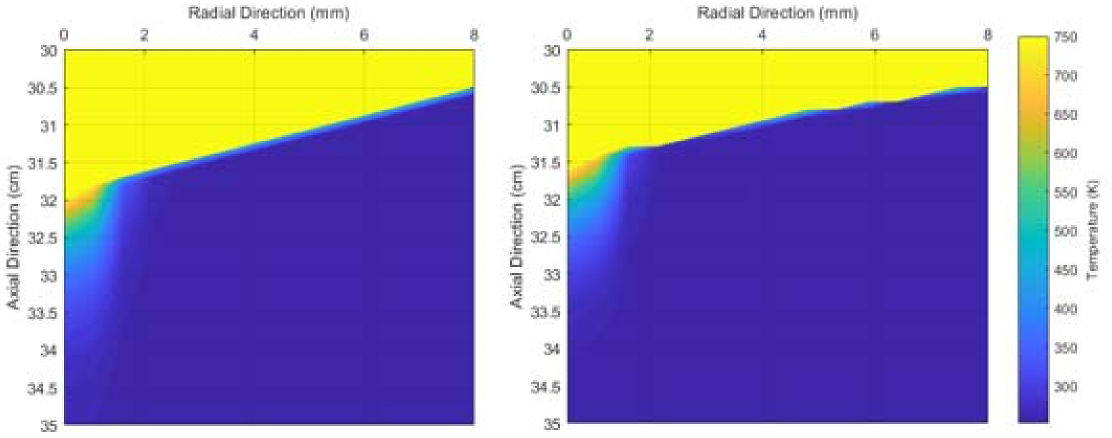

a) **No Break** b) **Break at 30 cm**

**Figure 19: Wire-Propellant Interaction Zone after 16 sec.**

In Figure 20 (a), at 16 sec, there is a slight change in the slope of the cone shown in the red circle and 4 seconds later, the slope has been propagated out. Of note, once the interaction zone returns to steady-state, the cone slope will return to the pre-break slope except for the small area shown in Figure 20 (b) which was affected by the break. Impacts of this burn area change are covered in section 4.6.

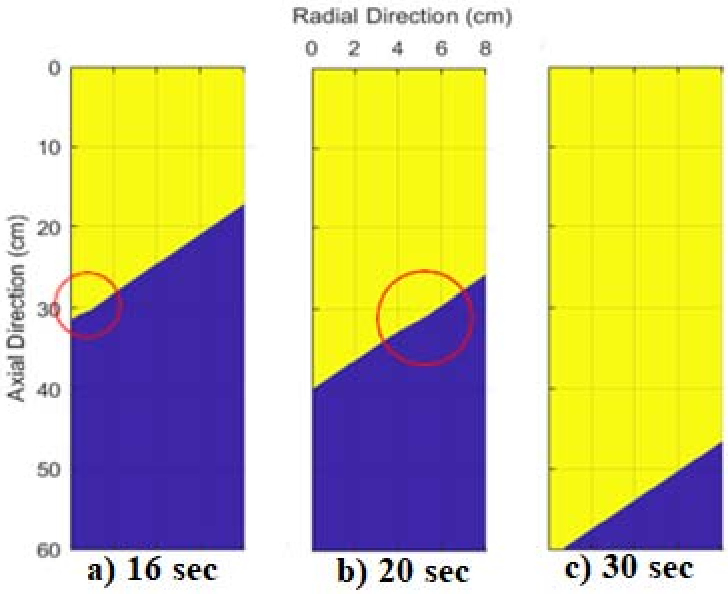

a) 16 sec b) 20 sec c) 30 sec

**Figure 20: Timeline of Burn Back for Broken Wire 30 cm.**

With wire thermal diffusivity identified as the leading contributor to increased burning rates along the wire, Figure 21 is used to provide a side-by-side comparison of each wire after 10 seconds of burning. Materials are arranged from highest to lowest thermal diffusivity. This figure supports findings from previous work and further validates the model used in this research. It also gives a glimpse at the potential for carbon nanotubes to rival performance of open internal tubes.

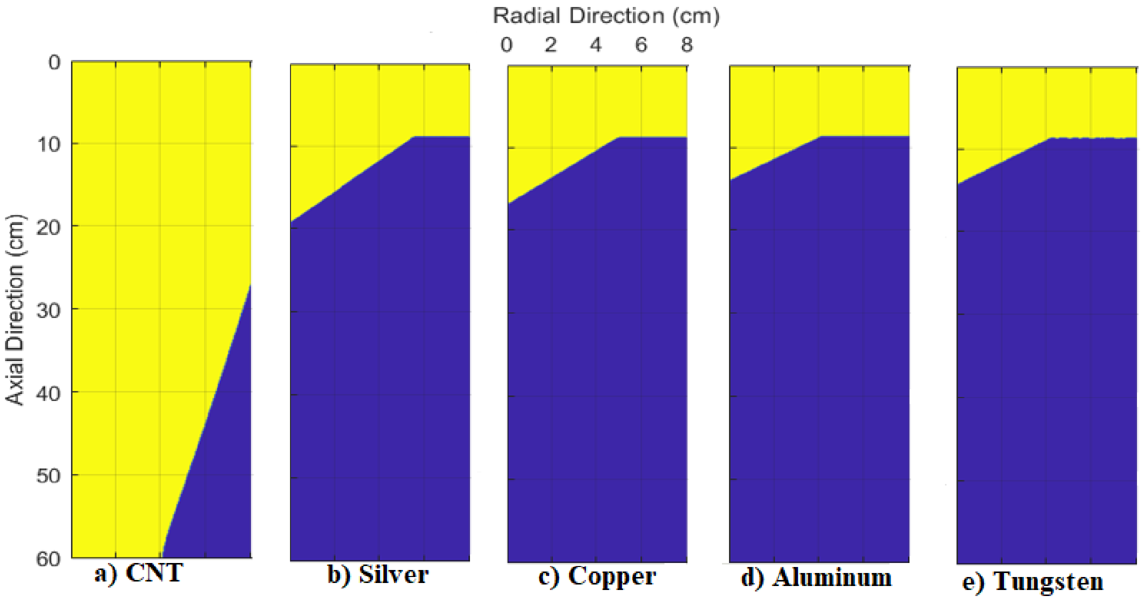

**Figure 21: Propellant Burn Back after 10 sec for each Wire Material.**

## 4.4 Wire Type

The five different wires mentioned in chapter three are compared while keeping the wire diameters the same at 2 mm. The first iteration of material testing produced the results in Table 9.

Table 9: Performance of Different Wire Materials.

| Material | Thermal Diffusivity ($10^{-4}$ m²/s) | Specific Impulse (s) | Total Impulse ($10^4$ N*s) | Action Time (s) | Max Pressure (MPa) | Average Pressure (MPa) | Max Thrust (N) | Average Thrust (N) |
|---|---|---|---|---|---|---|---|---|
| **No Wire** | - | 257.39 | 5.36 | 82.33 | 4.00 | 3.98 | 652.6 | 651.1 |
| **Nanocarbon** | 31.2 | 275.32 | 5.73 | 11.63 | 62.43 | 30.41 | 10,964.0 | 5,416.3 |
| **Silver** | 1.74 | 269.88 | 5.62 | 33.12 | 12.75 | 9.87 | 2,205.3 | 1,691.7 |
| **Copper** | 1.17 | 268.83 | 5.60 | 37.12 | 10.91 | 8.75 | 1,871.3 | 1,501.2 |
| **Aluminum** | 0.971 | 267.33 | 5.57 | 43.13 | 9.08 | 7.59 | 1,548.9 | 1,286.4 |
| **Tungsten** | 0.683 | 267.22 | 5.56 | 43.37 | 8.94 | 7.50 | 1,523.4 | 1,277.8 |

The addition of the wire is seen to greatly increase the pressure and thrust while cutting the burn time approximately in half or to about a seventh for CNT filament. These results are directly correlated to the thermal diffusivity of the wires and show higher thermal diffusivities will lead to improved performance. Figure 22 shows the potential to increase the total impulse by 7% for CNT and 5% for silver compared to a wireless end burner.

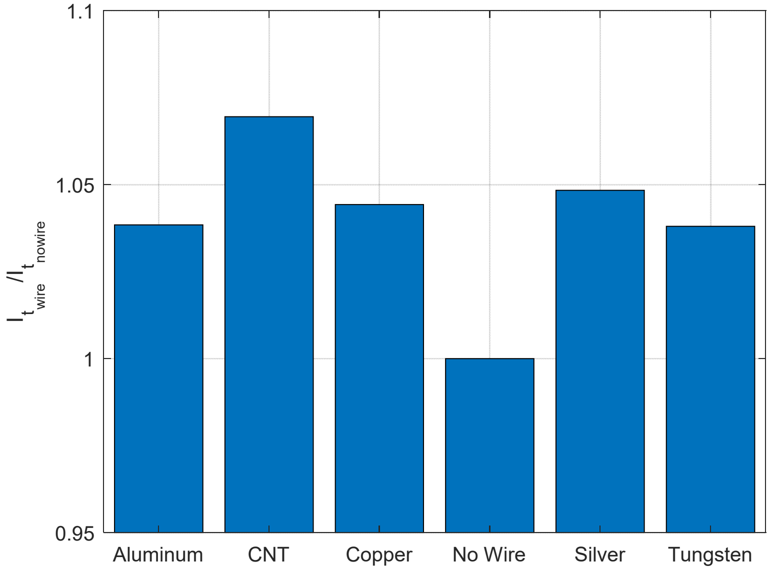

**Figure 22: Total Impulse Improvement for Wire Materials.**

Using Equation 89 to calculate the hoop stress encountered in the chamber walls,

$$\sigma_\theta = \frac{p_c R}{t} \tag{89}$$

where $p_c$ is the chamber pressure, $R$ is the inside radius of the wall (8 cm), and $t$ is the thickness of the wall (~2 mm), the max pressures are shown to produce stresses on the order of 300-2500 MPa for the wired scenarios. Tensile strengths for typical materials like titanium alloy, aluminum alloy 2024, alloy steel, and Kevlar 49 are 1240, 455, 1400-2000, and 1310 MPa respectively at 293 K [1]. It is important to note safety factors for tactical missile motors are often higher with the emphasis on reliability, long life, low cost, safety, ruggedness, and/or survivability [1]. However, the chamber pressures achieved from the increased burning rates are unsustainable for some. It is also desired in this research to maintain the same average chamber pressure for comparison purposes. As a reminder, the throat area used for this iteration of testing is 9.977x10$^{-5}$ m$^2$ and was found using the burn rate of 0.0073 m/s for the no-wire situation in Equation 90.

$$A_t = \frac{\dot{m}}{p_c}\frac{\sqrt{RT_{comb}}}{\sqrt{\gamma[2/\gamma+1]^{\gamma+1/\gamma-1}}} = \frac{A_b r p_b}{p_c}\frac{\sqrt{RT_{comb}}}{\sqrt{\gamma[2/\gamma+1]^{\gamma+1/\gamma-1}}} \tag{90}$$

To achieve a better comparison, the throat area is modified in an attempt to keep the chamber pressure similar to the desired operating pressure of 4 MPa for the wireless scenario. The next iteration of testing is conducted using throat areas shown in Table 10. The relative throat areas are seen to be inversely proportional to the action time. Comparing the results in Table 10, the specific and total impulse are shown to be approximately equal which is expected when the mass of the propellant and chamber pressure are held the same for each.

**Table 10: Performance of Wire Materials with New Throat Area.**

| Material | Relative Throat Area | Specific Impulse (s) | Total Impulse ($10^4$ N*s) | Action Time (s) | Max Pressure (MPa) | Average Pressure (MPa) | Max Thrust (N) | Average Thrust (N) |
|---|---|---|---|---|---|---|---|---|
| **No Wire** | 1 | 257.39 | 5.36 | 82.33 | 4.00 | 3.98 | 652.6 | 651.1 |
| **Nanocarbon** | 6.1 | 254.04 | 5.29 | 14.88 | 8.20 | 4.01 | 8,637.1 | 4,345.6 |
| **Silver** | 2.2 | 257.58 | 5.36 | 36.13 | 5.37 | 4.06 | 1,990.2 | 1,477.3 |
| **Copper** | 2 | 257.52 | 5.36 | 40.13 | 5.17 | 4.05 | 1,716.5 | 1,331.3 |
| **Aluminum** | 1.75 | 257.35 | 5.36 | 46.37 | 4.80 | 4.01 | 1,388.9 | 1,151.6 |
| **Tungsten** | 1.75 | 257.52 | 5.36 | 46.12 | 4.87 | 4.04 | 1,409.8 | 1,164.5 |

The impulse is slightly lower for CNT which is due to the average chamber pressure computation over the action time which cuts out some of the lower pressure values for CNT but not for the other wires. Since throat area adjustments are based off the average pressure calculations, the adjustment is overcorrected to where the thrust profile and impulses are slightly affected. The difference between materials can be seen in the thrust and pressure profiles in Figure 23.

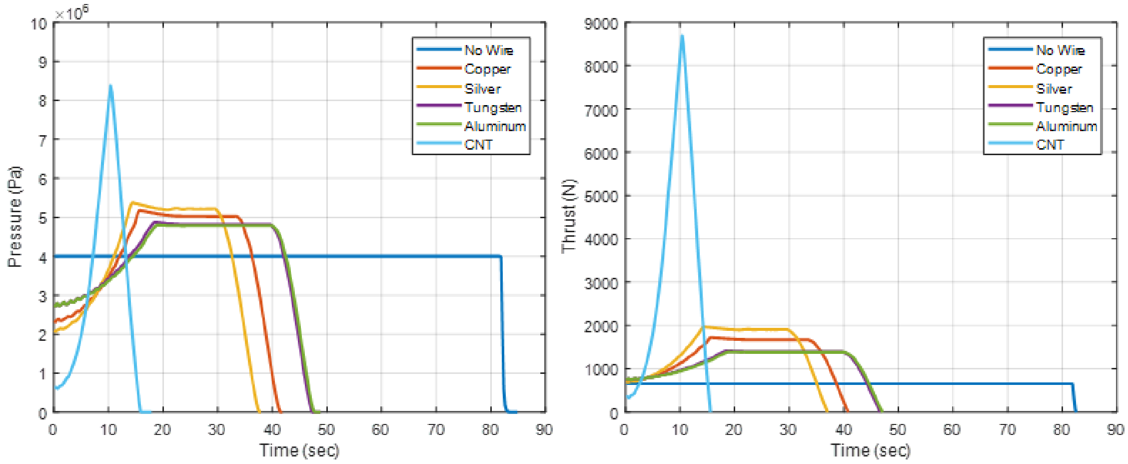

**Figure 23: Pressure and Thrust Profiles for $2^{nd}$ Iteration.**

From these results, CNT wires are shown to provide a significant amount of thrust in a short period of time which will be examined further in section 4.8 when comparing wired end burners to more traditional boost grains like the star and internal tube.

For this research, silver and CNT are selected as the best augmenting options. Silver is chosen as it is more readily available than CNT and for outperforming the other metallic wires as far as thrust and action time, while CNT is selected based on its massive thrust output.

### 4.5 Wire Size

With silver selected as a preferred material, the optimal geometry for the wire is determined. The throat area from the second iteration test is used for its closer representation to operating values. The wire diameters are varied from 1-10 mm and the profiles for each are depicted in Figure 24.

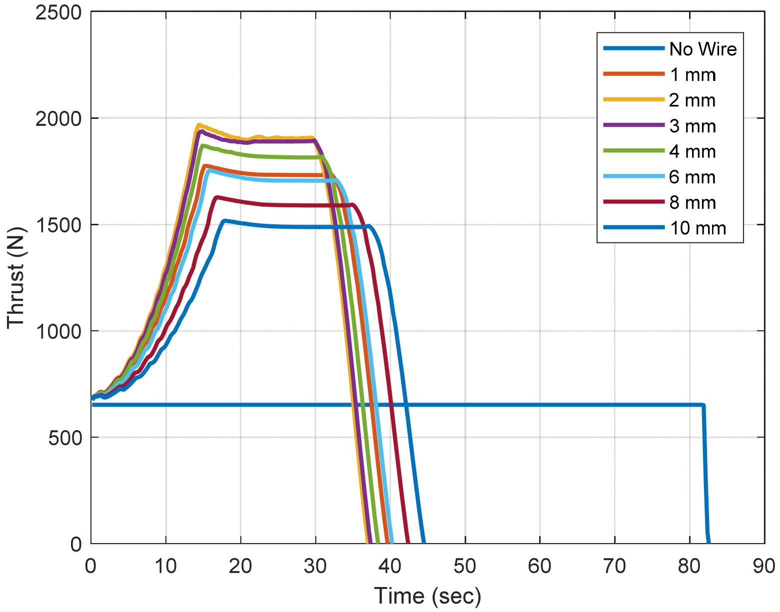

**Figure 24: Thrust Profile for Silver wire with various diameters.**

For diameters closer to 2 mm, the progressive burning region is shorter and neutral burning is achieved faster. This correlates to the increased heat flux into the propellant which opens the conical profile up more rapidly. The reason 2 mm is more optimal than 8 or 10 mm is while more heat flux is coming in for the larger wires, the heat leaves the wire faster due to increased surface area so there is less penetration to deep layers of propellant axially. Also, as the wire diameter increases, the assumption for being radially isothermal comes into question. Increasing the wire diameter will also slightly reduce the fill fraction as more space for propellant is taken up. Table 11 shows the results for total impulse, pressure, and thrust for each diameter.

**Table 11: Performance of Silver Wire with various Diameters.**

| Diameter (mm) | Total Impulse ($10^4$ N*s) | Action Time (s) | Max Pressure (MPa) | Average Pressure (MPa) | Max Thrust (N) | Average Thrust (N) |
|---|---|---|---|---|---|---|
| **1** | 5.33 | 38.88 | 4.88 | 3.80 | 1,781.3 | 1,367.0 |
| **2** | 5.36 | 36.13 | 5.37 | 4.06 | 1,990.2 | 1,477.3 |
| **3** | 5.36 | 36.63 | 5.29 | 4.03 | 1,980.4 | 1,459.1 |
| **4** | 5.34 | 37.63 | 5.12 | 3.92 | 1,881.6 | 1,416.1 |
| **6** | 5.32 | 39.38 | 4.82 | 3.73 | 1,757.6 | 1,341.8 |
| **8** | 5.29 | 41.63 | 4.49 | 3.53 | 1,629.6 | 1,265.1 |
| **10** | 5.22 | 43.63 | 4.21 | 3.36 | 1,519.7 | 1,196.5 |

Figure 25 shows the ideal diameter for the largest total impulse is right around 2 mm. While the optimal diameter is an order of magnitude more than King's optimal diameter for silver of 0.1 mm, the trend is identical with the rate falling off fairly quickly for smaller diameters and more gradually for larger diameters [8]. The trend also matches the model produced by Caveny and Glick for rectangular cross-sections (area of $1.29 \times 10^{-3}$ mm$^2$ or 0.02 mm equivalent diameter) and the experimental results from Rumbel *et. al.* which found a 0.127 mm diameter maximized the burn rate at 1000 psi [7, 15]. The difference in optimal diameters amongst the research can be attributed to the selected propellants having different thermal properties and temperature dependences, geometry of the propellant, and the methods used for each model. These results on wire size are significant because it shows the trends are similar and thus supporting the results in this research.

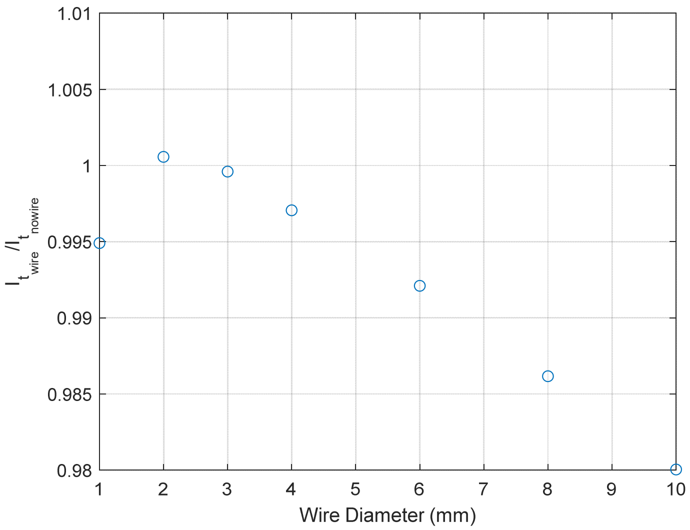

**Figure 25: Normalized Total Impulse for Silver wire with various diameters.**

### 4.6 Wire Break

With the optimal materials and size selected, a proper analysis of break location effects on performance can be conducted. A discontinuity in the wire is simulated at a 10-90% location along the wire. Figure 26 shows the thrust profile for each scenario and Figure 27 shows the difference in the thrust over time compared to a continuous wire.

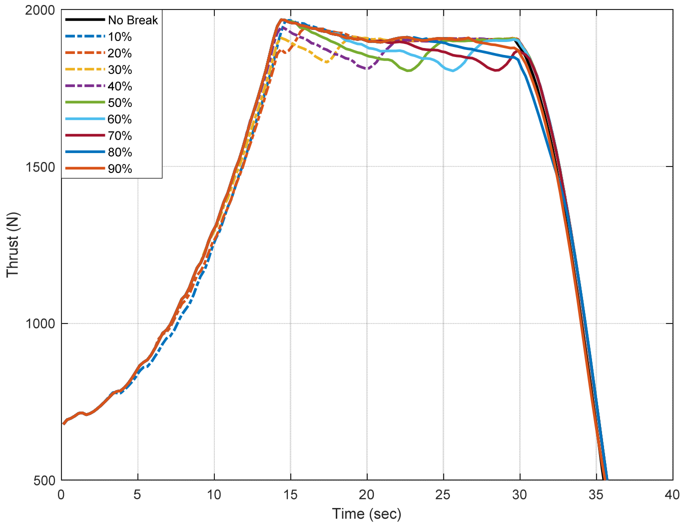

**Figure 26: Thrust Profile for Wires with Discontinuities.**

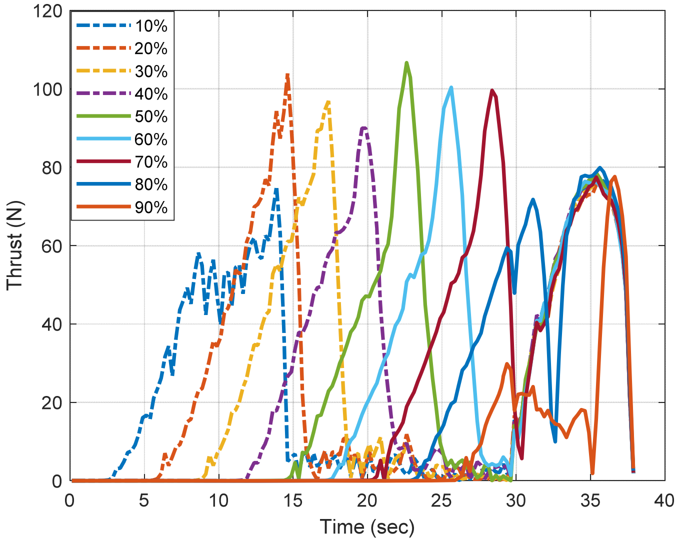

**Figure 27: Thrust Difference between Continuous and Discontinuous Wires.**

The figures show the discontinuity location has varying impacts to instantaneous thrust with the largest loss being 108 N (~6 % of thrust) and coming from breaks located between 20-70% into the wire. This is because neutral burning has already been achieved and the presence of the break will cause a deviation from the neutral burning. Identical simulations were conducted with a single CNT wire and the results were similar with instantaneous thrust loss of 6-8 %. Figure 28 shows having a wire break will only reduce the total impulse by roughly 0.5% and the total impulse does not vary with wire discontinuity location. This insignificant impact on performance demonstrates the reliability of wired configurations.

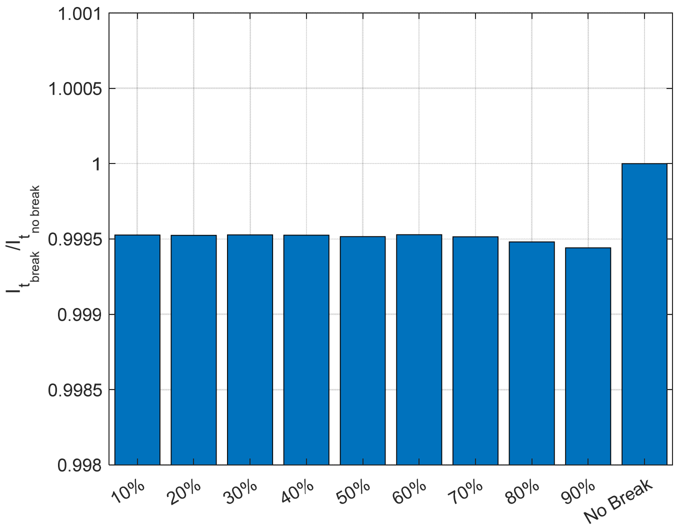

Figure 28: Total Impulse variations for each break location.

### 4.7 Multi-Wire

With results for the single wire configuration obtained, the multiwire configuration is evaluated for potential improvements. A 3-, 4-, 7-, and 19-wire grain are selected for their symmetrical fit in the missile case as well as to study the effect the number of wires has on performance. Silver is the tested material and the throat areas for each are adjusted to ensure the average chamber pressure is roughly equivalent. Shown in Table 12 are the results for the multi-wired scenarios.

**Table 12: Performance Comparison for Silver Single and Multiwire Configurations.**

| **Configuration** | **Relative Throat Area** | **Specific Impulse (s)** | **Total Impulse ($10^4$ N*s)** | **Action Time (s)** | **Max Pressure (MPa)** | **Average Pressure (MPa)** | **Max Thrust (N)** | **Average Thrust (N)** |
|---|---|---|---|---|---|---|---|---|
| **1 Wire** | 2.2 | 257.58 | 5.36 | 36.13 | 5.37 | 4.06 | 1,990.2 | 1,477.3 |
| **3 Wire** | 2.5 | 254.72 | 5.30 | 32.88 | 4.57 | 3.94 | 1,882.3 | 1,606.8 |
| **4 Wire** | 2.5 | 254.42 | 5.30 | 32.38 | 4.58 | 4.00 | 1,885.1 | 1,629.3 |
| **7 Wire** | 2.55 | 255.54 | 5.32 | 31.63 | 4.47 | 4.02 | 1,876.8 | 1,674.1 |
| **19 Wire** | 2.65 | 254.36 | 5.28 | 30.63 | 4.31 | 3.98 | 1,874.8 | 1,717.7 |

The impulses are slightly lower for the multiwire configurations due to the method estimation method for finding mass generation in the "empty" volume mentioned in section 3.4.5. The trends shown in the average thrust are useful as it shows increasing the number of wires will provide higher thrust for longer time. Figure 29 shows, on average, multiwire configurations arrive at neutral burning 10 seconds faster than the single wire. This is attributed to the shortened radius of each tube which will take less time to reach the full cone shape.

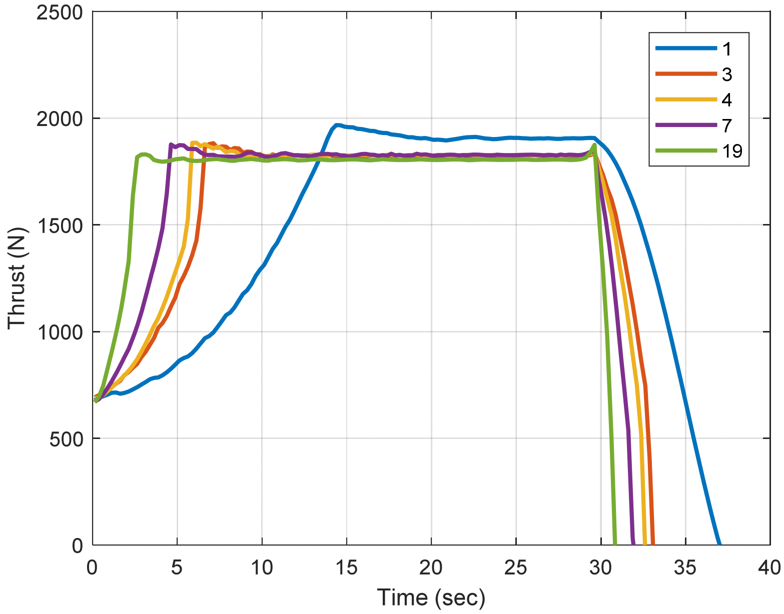

**Figure 29: Thrust Profiles for Silver Single and Multiwire Configurations.**

Now looking at the multiwire configuration with one wire having a discontinuity, the performance impact on thrust, total impulse, and center of mass change are analyzed. Figure 30 shows the thrust profiles for a continuous 7-wire configuration and a 7-wire configuration with one discontinuity at 50% of its length.

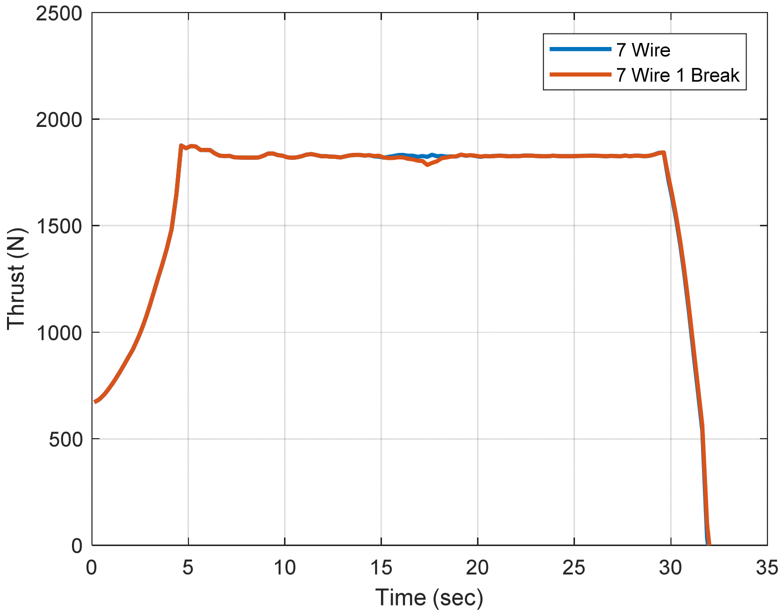

**Figure 30: Performance Comparison of Continuous and Discontinuous 7-wire Configuration.**

Compared to the 180 N loss for a single wire break, the maximum instantaneous drop in thrust for a single discontinuity at the half way point on the wire produces a thrust loss of 40 N (~2% of thrust) for the 7-wire grain. Table 13 shows increasing the number of wires will decrease the impact one wire break has on thrust. However, it is assumed more wires will increase the likelihood of the presence of a discontinuity.

**Table 13: Relationship between One Wire Break in Multiwire Configurations.**

| **Configuration** | **Max Instantaneous Thrust Loss (N)** | **Percent Loss** |
|---|---|---|
| **1 Wire** | 180 | 9.04 |
| **3 Wire** | 80 | 4.25 |
| **4 Wire** | 60 | 3.18 |
| **7 Wire** | 40 | 2.13 |
| **19 Wire** | 20 | 1.07 |

To identify potential shifts in center of gravity, the unburned mass is tracked to determine if significant mass variations occur when a wire discontinuity is present. The break is assumed to be on an outer wire since the center wire is ideally in line with the

CG and, through symmetry and assuming a linear wire break, would experience no change in CG location.  Figure 31 shows the difference in mass between continuous and discontinuous multiwire configurations at any time of the flight.  The difference in mass is the additional mass around the broken wire tube due to the burning surface area change experienced by slowed burning rates along the wire near at the gap.  The max difference is approximately between 0.006-0.034 kg with one break on an outer wire.  Considering the total mass of the missile is roughly 150 kg, or 129 kg after all the propellant is burned up, this slight difference is considerably small and the center of mass is assumed to not shift radially.  Figure 32 provides a better visual showing the difference is practically unobservable.

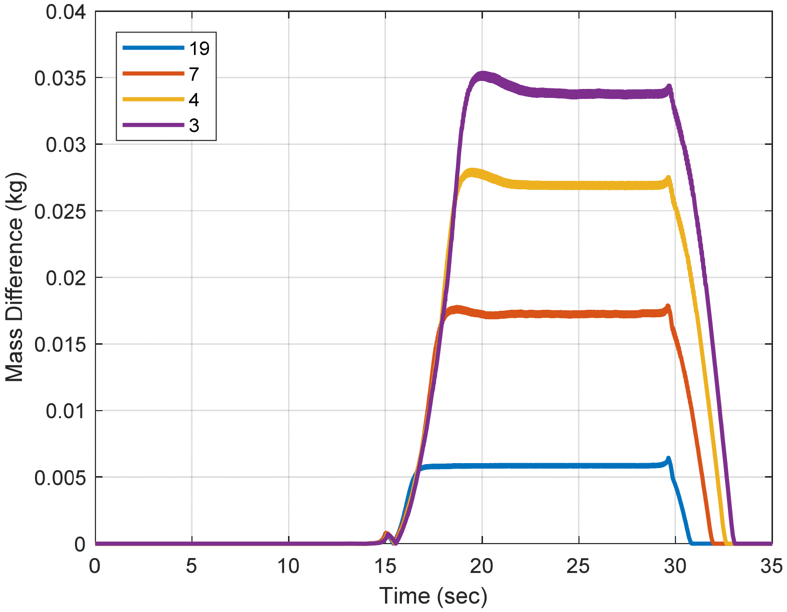

**Figure 31: Difference in Mass between a Continuous and Discontinuous (Break at 50%) Multiwire Configurations.**

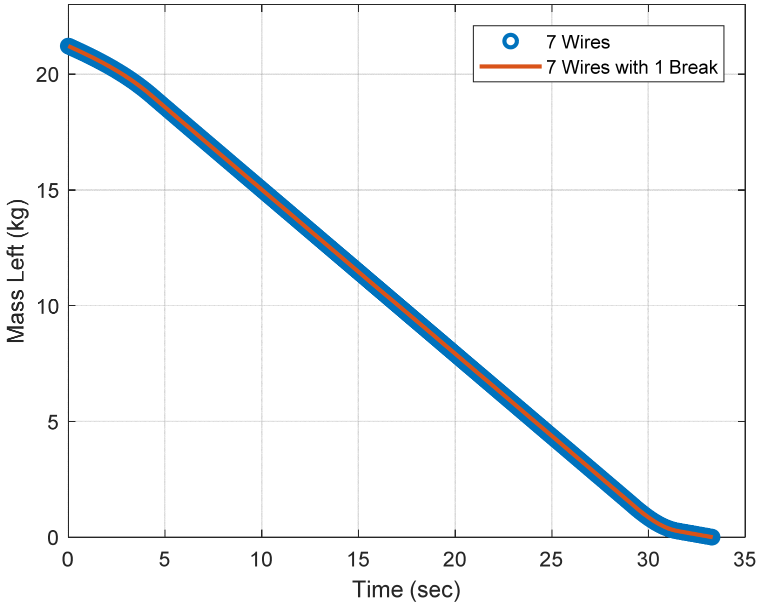

**Figure 32: Unburned Propellant Remaining over time.**

### 4.8 Internal Tube and Star

Typical air-launched rocket motors actually benefit from a reducing thrust with burn time [1]. A high thrust is desired up front to accelerate the missile to flight speed but as the mass of the vehicle decreases, lower thrust often reduces drag losses and permits a more effective flight path [1]. For this reason, the internal tube and 5-point star configuration are more commonly used designs to provide the high thrust in the boost phase which is usually followed up with an end burner or other low thrust producing grains for the sustaining phase. Results for these two configurations can provide some perspective on the previous results. Performance for wireless, single wire, 7 wire, internal tube, and 5-point star configurations are compared in Table 14 to fully identify the top performers. The throat areas are adjusted to achieve comparable average chamber pressures.

**Table 14: Performance for Various Grain Types.**

| Configuration | Relative Throat Area | Specific Impulse (s) | Total Impulse ($10^4$ N*s) | Action Time (s) | Max Pressure (MPa) | Average Pressure (MPa) | Max Thrust (N) | Average Thrust (N) |
|---|---|---|---|---|---|---|---|---|
| **No Wire** | 1 | 257.39 | 5.36 | 82.33 | 4.00 | 3.98 | 652.60 | 651.10 |
| **1 Wire (Silver)** | 2.2 | 257.58 | 5.36 | 36.13 | 5.37 | 4.06 | 1,990.2 | 1,477.3 |
| **1 Wire (CNT)** | 6.1 | 254.04 | 5.29 | 14.88 | 8.20 | 4.01 | 8,637.1 | 4,345.6 |
| **7 Wire (Silver)** | 2.55 | 255.54 | 5.32 | 31.63 | 4.47 | 4.02 | 1,876.8 | 1,674.1 |
| **7 Wire (CNT)** | 9.5 | 260.66 | 5.42 | 9.88 | 5.92 | 3.98 | 9,417.8 | 6,496.6 |
| **Internal Tube** | 9.2 | 257.49 | 5.03 | 8.28 | 6.42 | 4.01 | 10,032.0 | 6,085.5 |
| **Star** | 16 | 257.69 | 4.22 | 4.00 | 4.03 | 4.01 | 10,522.0 | 10,490.0 |

The silver wired configurations are shown to provide an intermediate level of performance between the open internal configurations and the unmodified end burner. With this information, wired configurations could find use in an application requiring more thrust than an end burner and longer burn times than the internal tube or star grains. CNT, however, appears as a strong candidate to replace current boost phase designs. It can potentially deliver the desired high thrust over a short time while providing more total impulse due to the higher fill fraction. Table 14 shows single wire CNT produces the largest max chamber pressure, however, this can be mitigated several ways. The diameter of the wire can be adjusted to slow burning rates along the propellant, a propellant with different thermal properties could be used, or throat area could be adjusted to allow more mass flow and reduce chamber pressure. The thrust profiles for each configuration are shown in Figure 33. It appears the single wire CNT configuration never produces a neutral burning region which is explained by geometry. What is happening is the heat from the wire is penetrating all the way to the end of the case before the radial burning from the initial opening reaches the side walls and therefore a constant cone shape is never developed. If a higher L/D were to be selected, a neutral burning region could develop, which is shown in the 7 wire CNT profile.

A significant finding in this research is the thrust profile produced by CNT is similar to the star grain and internal tube and by analyzing the total impulse of each, we see the single and 7-wire configuration can provide ~28 % and ~25 % more total impulse than the star grain and ~9% and ~5 % more than the internal tube. This shows range can likely be improved when using CNT embedded grains over internal and star grains.

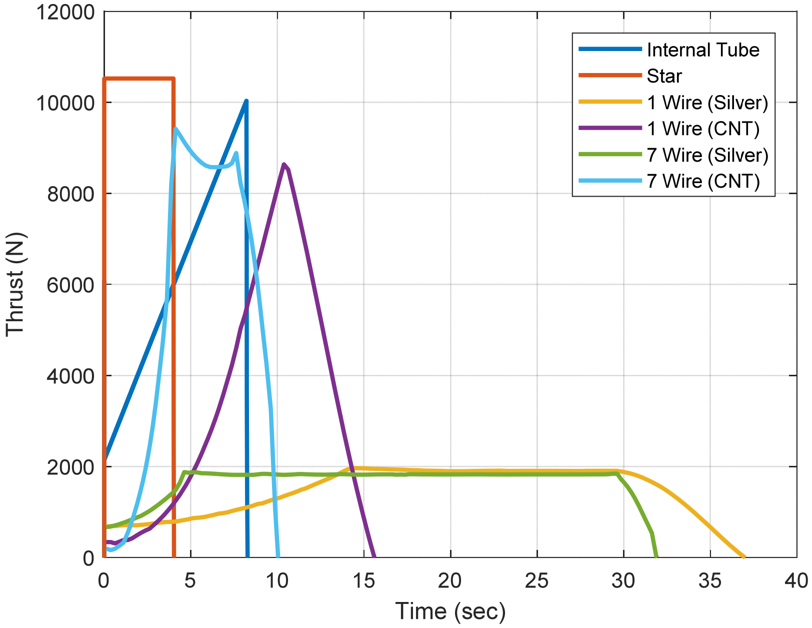

**Figure 33: Pressure and Thrust Profiles for Various Grains.**

### 4.9 Propellant and Altitude Variations

As the use of air-to-air missiles is not limited to one altitude, simulations are run at several altitudes to show how performance will vary. The single silver wire configuration is used with only ambient pressure and temperature changing per test. Figure 34 shows the thrust profiles while operating at altitudes of 3-12 km (10-40 kft). By examining Equation 6 for thrust, the thrust output is dependent on the ambient pressure. Ambient pressure is lower at higher altitudes so it is expected to have better performance at higher altitudes and lower performance at lower altitudes which is demonstrated in Figure 34.

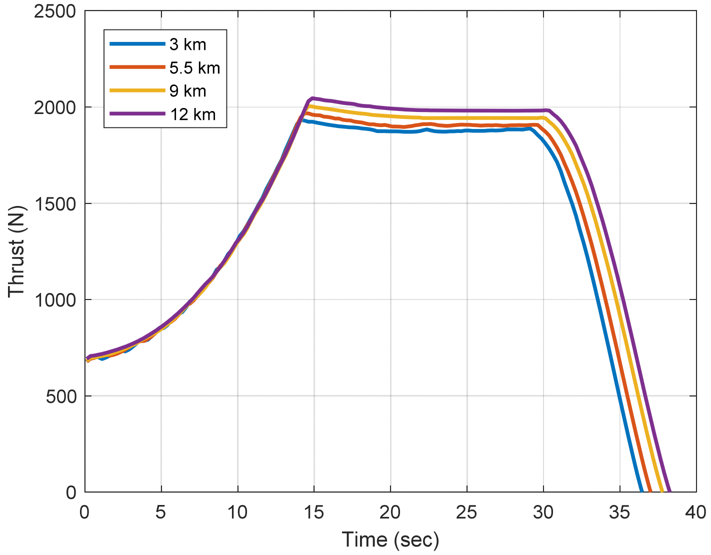

**Figure 34: Thrust Profile for Single Silver Wire Configuration at Varying Altitudes.**

For all the previous simulations, the propellant properties were held constant to measure the effects of different wired configurations. Now, the propellant properties are adjusted to determine the effect of thermal diffusivity and the burning characteristics (temperature coefficient, temperature sensitivity, burning rate exponent). To test the effect of thermal diffusivity, all properties for the First-Stage Minuteman 1 propellant are held constant except for the thermal conductivity. Figure 35 shows the thrust profile for each iteration. Initially, one might think having higher thermally diffusive propellant would increase the burning along the wire, however, the lower diffusivity allows the wire to heat up more axially which, in the time, will give higher burning rates, larger cone surface area, and more thrust.

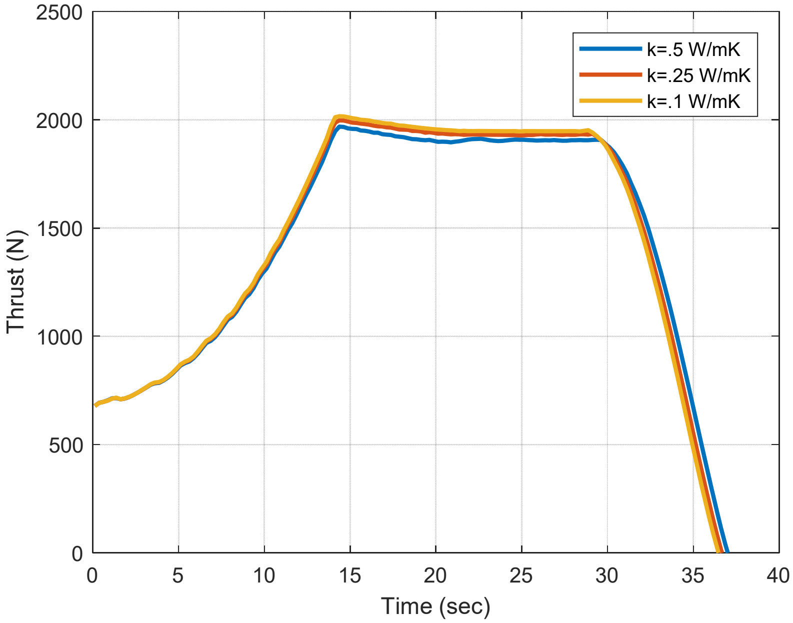

**Figure 35: Propellant Thermal Diffusivity Impact on Thrust Profile with a Single Silver Wire.**

To measure the effects of temperature coefficient, temperature sensitivity, and burning rate exponent, a new propellant is selected to compare with the Minuteman propellant. The properties for the new propellant are shown in Table 15 [1, 3].

**Table 15: Properties for Operational Solid Propellant.**

| Property | Propellant |
|---|---|
| **Composition** | 29% Nitroglycerine (NG)<br>21.9% Nitrocellulose (NC)<br>21.1 % Al<br>20.4% AP<br>7.6% Stabilizer/Binder |
| **Density (kg/m³)** | 1880 |
| **Thermal Conductivity (W/mK)** | 0.25 |
| **Gas Constant, R (J/kgK)** | 273.03 |
| **Specific Heat Capacity (J/kgK)** | 1550 |
| **Burning Rate (mm/s) @ 4 MPa** | 7.3 |
| **Temperature Sensitivity, (°K)** | 1.3E-03 |
| **Burning Rate Exponent** | 0.4 |
| **Temperature Coefficient (m/sPa$^{0.4}$)** | 1.67E-05 |
| **Adiabatic Flame Temperature (K)** | 3880 |

To help isolate the impact of the propellant properties, the burn rate at 4 MPa and grain temperature of 252 K is assumed to be equal for both (7.3 mm/s) which gives a temperature coefficient of $1.67\text{x}10^{-5}$ m/sPa$^{0.4}$ for the new propellant. However, as the temperature of the propellant increases along the wire, the burn rates will no longer remain equal since the temperature coefficients, sensitivities, and burn rate exponents are different. The relationship between the burn rate and the aforementioned terms is reiterated in Equation 91.

$$r = a_o e^{\sigma_p (T_b - T_{0b})} p_c^n \tag{91}$$

The temperature sensitivity $\sigma_p$ and temperature coefficient $a_o$ are higher for the Minuteman propellant and the burn rate exponent is higher for the selected CMDB propellant. Figure 36 shows the thrust profiles for each. At an average chamber pressure of 4 MPa, the Minuteman propellant is shown to produce higher thrust and achieve neutral burning faster which is attributed to the higher increase in burning rates along the wire compared to the CMDB mixture. The CMDB propellant does have the higher burn rate exponent so, at some higher chamber pressure, it is predicted to eventually surpass the burning rate of the Minuteman mixture. Overall, propellants with naturally higher burning rates are projected to benefit more from wired configurations since the components which comprise the burning rate equation tend to be larger already, especially temperature sensitivity as it can amplify or dampen the temperature difference shown in Equation 91. More testing is required to better quantify these statements.

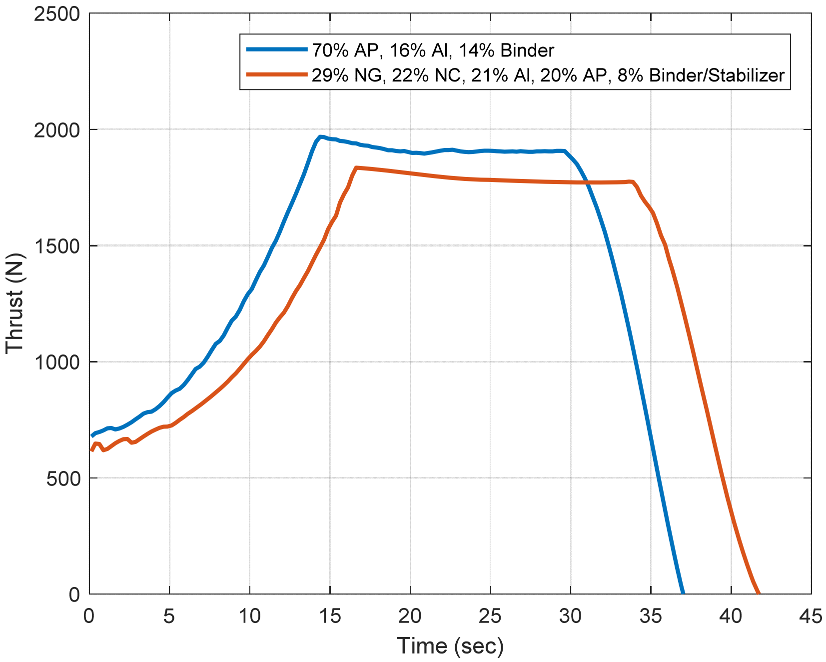

**Figure 36: Thrust Profile for First-Stage Minuteman 1 and CMDB with a Single Silver Wire.**

### 4.10 Summary

The results from section 4.4 and 4.5 on wire size and material agree with past experimental data and previous models. These results are used to validate the model and provide some measurements for comparison with the other grain configurations. The conclusion on wire breaks is they have little impact on the overall performance which helps bolster the argument for the reliability of wired configurations. Finally, carbon nanotubes are identified, from a thermal diffusivity perspective, as providing performance which potentially rivals radially burning configurations.

# V. Conclusions and Recommendations

## 5.1 Chapter Overview

This chapter covers the conclusions and impacts this research has on the potential of wire-embedded end burners. Recommendations for future work are provided as well.

## 5.2 Conclusions of Research

Based on the data presented in chapter 4, wired configurations are shown to provide more thrust over a shorter action time which could prove useful in boost-sustain applications. A single wire discontinuity is shown to have little impact on total impulse but will cause a 1-8% loss in instantaneous thrust, depending on the number of wires in the configuration, when the burning surface reaches the break. Multiwire configurations provide even shorter burn times and more thrust. Wire discontinuities in the outer wires are shown to not negatively impact the burning area enough to cause significant movement of the center of mass. Lastly, carbon nanotube fibers are shown to increase burning rates up to 7 times more than a wireless end burner and thus produce thrust profiles comparable to internal tubes and star grains. With the parameters used for this research, total impulse can potentially be improved by 25% over radially burning grains.

## 5.3 Significance of Research

This research builds upon existing work which proves wires embedded in propellant enhance the burning rate along the wire. While only gaps between the wire and propellant having been considered before, this research examines the presence of wire discontinuities on performance. The research shows small thrust losses will be experienced and should have minimal impact to flight performance. This research also highlights potential future use of CNT in solid propellants by demonstrating performance comparable to existing grains.

### 5.4 Recommendations for Future Research

As carbon nanotube technology has developed, the identified applications for it have grown immensely. While wire-embedded experimental testing has been completed several times for metallic wires, it has never been done for carbon nanotubes. The results for this research suggest CNT have the potential to produce thrust profiles similar to open internal grains and being composed of carbon indicates it can provide positive impacts to combustion as well while not producing liquid or chunks of metal in the exhaust. It would be very intriguing to see strand tests completed with CNT embedded propellants to verify or contradict the results in this research.

This model could also be extended to include gaps between the wire and propellant and account for transient temperatures during start up to mimic reality more closely. Also, the practice of casting and extruding propellants is not perfect and it is expected the wire will not always be perfectly parallel with the missile. Significant modifications could be made to the code to simulate bent or nonlinear wires as assumed in this research.

# Appendix A: Main Code

```
% Wilson_Thesis.m
% Computes performance for wireless, single-, and multi- wire end burning
% grains with or without breaks in the wire.
clear all; clc; close all;
% Configuration Desired
Wire=1; % Select 0 for Wireless or 1 for Single Wire/Multi-Wire
MultiWire=0; % Select 0 for Wireless or Single Wire Grain and Select #>0 for
Multiwire
Break=0; % Select 1 for break, 0 for no break
Break_L=300; % Node Location of break
Break_U=Break_L+1;
% Matrix
R_case=.08; % Radius of Case (m)
R_max=.08; % Radius of Propellant (m) .0265 (43), .08 (150), .037 (64), .0155
(21), .033 (56)
Z_max=.6;   % Length of Propellant (m)
R_wire=.001;% Radius of Wire (m)
i_max=150;   % # of Nodes in Radial Direction
j_max=601;  % # of Nodes in Axial Direction
dr=(R_max-.005)/(i_max); % Radial Step (m)
dz=Z_max/(j_max-1); % Axial Step (m)
if Wire==0
    i_max=161;
    dr=R_max/(i_max-1);
    r=linspace(0,R_max,i_max); % Location of Nodes in Radial Direction
else
    r=linspace(.0055,R_max,i_max); % Location of Nodes in Radial Direction
end
z=linspace(0,Z_max,j_max);     % Location of Nodes in Axial Direction
% Time
dt=.001;    % Time step (s)
t_step=35000; %# of Time Steps
% Wire and Propellant Initialization
% Density(kg/m^3), Thermal Conductivity(W/mK), Specific Heat Cap.(J/kgK),
Emissivity, Melting Temp.(K)
% Silver
p_wire=10500; k_wire=429; Cp_wire=235; e_wire=.02; T_melt=1235;
% Copper
%p_wire=8933; k_wire=401; Cp_wire=385; e_wire=.03; T_melt=1358;
% Aluminum
%p_wire=2702; k_wire=237; Cp_wire=903; e_wire=.04; T_melt=933;
% Tungsten
%p_wire=19300; k_wire=174; Cp_wire=132; e_wire=.04; T_melt=3660;
% Nano Carbon
%p_wire=1300; k_wire=3000; Cp_wire=740; e_wire=.98; T_melt=2600;
% Propellant
```

```
p_prop=1760.44; k_prop=.502; Cp_prop=1551;
omega=5.67E-8; % Stephan-Boltzmann constant (W/m^2T^4)
g=9.8066; % Standard Earth Gravitional Acceleration (m^2/s)
alpha_wire=k_wire/(p_wire*Cp_wire); % Thermal Diffusivity of Wire (m^2/s)
alpha_prop=k_prop/(p_prop*Cp_prop); % Thermal Diffusivity of Prop (m^2/s)
Fo_zw=alpha_wire*dt/dz^2; % Fourier # for wire in Axial Direction
Fo_zp=alpha_prop*dt/dz^2; % Fourier # for prop in Axial Direction
Fo_rp=alpha_prop*dt/dr^2; % Fourier # for prop in Radial Direction
% Temperature Initialization
T_comb=3472;    % Combustion Temp. or Adiabatic Flame Temp. of Prop. (K)
T_int=252;  % Ambient Temp. at 5.5 km and Initial Prop. Temp. (252 @5.5)
(229.74 @9) (216.66 @12) (268.67 @3)
T=T_int*ones(length(r),length(z));  % Nodes Initializaed to Ambient Temp.
% Chamber and Ambient Conditions Initialized
P_c=4E6;    % Desired Operating Chamber Pressure (Pa)
P_2=50539;  % Initial Pressure at Exit (Pa) (50539 @5.5) (30800 @9) (19399 @12)
(70121 @3)
P_amb=P_2;  % Ambient Pressure at 5.5 km (Pa)
P2_Pc=P_2/P_c; %Pressure Ratio of Exit/Chamber
gamma=1.17; % Specific Heat Ratio for Gas Mixture in Chamber
R=283.77;   % Gas Constant for Gas Mixture in Chamber (J/kgK)
C=5; % Throat Area Multiplier for adjusting area relative to the wireless grain
br=0.0073; % Burn Rate of Prop used in this research for wireless grain at the
stated P_c and T_int above (m/s)
A_t=((pi*R_case^2*C*br*p_prop)/(P_c))*sqrt((R*T_comb)/(gamma*(2/(gamma+1))^((ga
mma+1)/(gamma-1)))); % Throat Area (m^2)
A_2=A_t/(((gamma+1)/2)^(1/(gamma-
1))*((P2_Pc)^(1/gamma))*sqrt(((gamma+1)/(gamma-1))*(1-(P2_Pc)^((gamma-
1)/gamma))));
r_t=sqrt(A_t/pi); % Throat Radius (m)
h=.1; % Length Between Throat and Initial Prop Surface (m)
V_c=(pi*h/12)*((2*R_case)^2+4*R_case*r_t+(2*r_t)^2); % Initial Chamber Vol
(m^3)
m_c=P_c*V_c/(R*T_comb); % Initial Mass in Chamber (kg)
m_out=0; % Initial Mass Flow out of Nozzle (kg/s)
% Burn Rate Initialized
br=zeros(length(r),length(z)); % Axial Burn Rate Initialized
br_r=zeros(length(r),length(z)); % Radial Burn Rate Initialized
burn_distance=0*br; % Axial Burn Distance Initialized
burn_distancen=0*br; % Axial Burn Distance Initialized
burn_distance_r=0*br; % Radial Burn Distance Initialized
burn_distancen_r=0*br; % Radial Burn Distance Initialized
% Mass Initialized
m=zeros(length(r),length(z)); % Matrix created for Mass
[m,Total_Mass]=int_mass(Wire,m,p_prop,p_wire,i_max,j_max,dr,dz,R_wire,r); %
Mass Matrix Initialized (kg)
if MultiWire==0
    Total_Mass=Total_Mass;
```

```
else
    Total_Mass=MultiWire*Total_Mass+p_prop*(pi*Z_max*R_case^2-
MultiWire*pi*Z_max*R_max^2); % Mass for total # of tubes plus mass not
considered in the matrix
end
m_int=m; % Renamed for Looping purposes
% COMBUSTION BOUNDARY CONDITION
e_comb=.8;  % Emissivity of Comustion Gas Mixture
h=e_comb*omega*(T_comb+T_int)*(T_comb^2+T_int^2); % Estimated Convection
Coefficient (W/m^2K)
Bi_prop=(h*dz)/k_prop; % Biot Number for Prop
Bi_wire=(h*dz)/k_wire; % Biot Number for Wire
% Performance Loop
gen=zeros(1,t_step); % Mass Generated Vector Initialized
time=zeros(1,t_step); % Time Vector Initialized
Exit_Velocity=zeros(1,t_step); % Exit Velocity Vector Initialized
Mdot_v=zeros(1,t_step); % Nozzle Mass Flow Vector Initialized
Pressure=zeros(1,t_step); % Chamber Pressure Vector Initialized
Thrust=zeros(1,t_step); % Thrust Vector Initialized
Total_m_Left=zeros(1,t_step); % Prop Mass Remaining Vector Initialized
for k=1:t_step
    [T] =
Temperature(Wire,m,Fo_zw,Fo_zp,Fo_rp,T,i_max,j_max,Bi_wire,p_prop,Cp_prop,T_com
b,r,dz,R_wire,p_wire,Cp_wire,k_wire,dr,dt,k_prop,h,alpha_prop,e_wire,omega,Brea
k,Break_L,Break_U,T_melt);

[m,burn_distance,Total_Mass_Left,br,br_r,m_gen,m_dot_gen,burn_distancen,burn_di
stancen_r]=new_mass(Wire,MultiWire,m,i_max,j_max,dz,dr,br,dt,T,P_c,burn_distanc
e,burn_distancen,burn_distance_r,burn_distancen_r,m_int,br_r,p_prop,r,z,T_melt,
R_wire,R_case,R_max);
    gen(k)=m_gen;
    Total_m_Left(k)=Total_Mass_Left;

[m_dot_out,P_c,m_c,V_c,v_exit,F,P_2]=Chamber(m_c,m_gen,A_t,gamma,R,T_comb,V_c,p
_prop,dt,P_2,P_amb,A_2,P_c,P2_Pc);
    time(k)=dt*k;
    Exit_Velocity(k)=v_exit;
    Mdot_v(k)=m_dot_out;
    Pressure(k)=P_c;
    Thrust(k)=F;
    k
end
% Unfiltered data
indices = find(Thrust>0); % Time when Thrust is greater than 0
It=sum(dt.*Thrust(indices(1):indices(end))); % Total Impulse (N*s)
Isp=It/(Total_Mass*g); % Specific Impulse (s)
indices = find((Thrust-.1*max(Thrust))>=0);
action_time_Thrust=time(indices(end));
```

```
ave_Thrust=sum(Thrust(indices(1):indices(end)))/length(Thrust(indices(1):indice
s(end)));
indices = find((Pressure-.1*max(Pressure))>=0);
action_time_Pressure=time(indices(end));
ave_Pressure=sum(Pressure(indices(1):indices(end)))/length(Pressure(indices(1):
indices(end)));
Max_Thrust=max(Thrust); % Max Thrust
Max_Pressure=max(Pressure); % Max Pressure
% Filtered data
k=251; % # of steps to be averaged
p=2;
time_n=linspace(dt,t_step,t_step/250); % New Time Vector Initialized
Exit_Velocity_n=zeros(1,t_step/250); % New Exit Velocity Vector Initialized
Thrust_n=zeros(1,t_step/250); % New Thrust Vector Initialized
Pressure_n=zeros(1,t_step/250); % New Pressure Vector Initialized
Mdot_n=zeros(1,t_step/250); % New Nozzle Mass Flow Vector Initialized
while k<=t_step
    time_n(1)=sum(time(1:250))/250;
    time_n(p)=sum(time(k:k+249))/250;
    Exit_Velocity_n(1)=sum(Exit_Velocity(1:250))/250;
    Exit_Velocity_n(p)=sum(Exit_Velocity(k:k+249))/250;
    Thrust_n(1)=sum(Thrust(1:250))/250;
    Thrust_n(p)=sum(Thrust(k:k+249))/250;
    Pressure_n(1)=sum(Pressure(1:250))/250;
    Pressure_n(p)=sum(Pressure(k:k+249))/250;
    Mdot_n(1)=sum(Mdot_v(1:250))/250;
    Mdot_n(p)=sum(Mdot_v(k:k+249))/250;
    k=k+250;
    p=p+1;
end
indices = find(Thrust_n>0);
It_f=sum(250*dt.*Thrust_n(indices(1):indices(end))); % Filtered Total Impulse
Isp_f=It_f/(Total_Mass*g); % Filtered Specific Impulse
indices = find((Thrust_n-.1*max(Thrust_n))>=0);
action_time_Thrust_n=time_n(indices(end));
ave_Thrust_n=sum(Thrust_n(indices(1):indices(end)))/length(Thrust_n(indices(1):
indices(end)));
indices = find((Pressure_n-.1*max(Pressure_n))>=0);
action_time_Pressure_n=time_n(indices(end));
ave_Pressure_n=sum(Pressure_n(indices(1):indices(end)))/length(Pressure_n(indic
es(1):indices(end)));
Max_Thrust_n=max(Thrust_n); % Max Filtered Thrust
Max_Pressure_n=max(Pressure_n); % Max Filtered Pressure
```

# Appendix B: Initial Mass Function

```
% int_mass.m
% Calculates Initial Mass for each node and sums them for a total initial
% mass.
function [m,Total_mass] =
int_mass(Wire,m,p_prop,p_wire,i_max,j_max,dr,dz,R_wire,r)

if Wire==0 % Initial Mass for Wireless Grain.
% Center Line Mass
    for i=1
        for j=1
            m(i,j)=.5*p_prop*pi*dz*(dr/2)^2;
        end
        for j=2:j_max-1
            m(i,j)=p_prop*pi*dz*(dr/2)^2;
        end
        for j=j_max
            m(i,j)=.5*p_prop*pi*dz*(dr/2)^2;
        end
    end
% Side Wall Mass
    for i=i_max
        for j=1
            m(i,j)=.5*p_prop*pi*dz*(r(i)^2-(r(i)-dr/2)^2);
        end
        for j=2:j_max-1
            m(i,j)=p_prop*pi*dz*(r(i)^2-(r(i)-dr/2)^2);
        end
        for j=j_max
            m(i,j)=.5*p_prop*pi*dz*(r(i)^2-(r(i)-dr/2)^2);
        end
    end
% Internal Mass
    for i=2:i_max-1
        for j=1
            m(i,j)=.5*p_prop*pi*dz*((r(i)+dr/2)^2-(r(i)-dr/2)^2);
        end
        for j=2:j_max-1
            m(i,j)=p_prop*pi*dz*((r(i)+dr/2)^2-(r(i)-dr/2)^2);
        end
        for j=j_max
            m(i,j)=.5*p_prop*pi*dz*((r(i)+dr/2)^2-(r(i)-dr/2)^2);
        end
    end
    % Initial Total Mass
    Total_mass=0;
    for i=1:i_max
```

```
        for j=1:j_max
            Total_mass=Total_mass+m(i,j);
        end
    end
elseif Wire==1 % Initial Mass for Single Wire Grain.
% Mass of Wire
    for i=1
        for j=1
            m(i,j)=.5*p_wire*pi*dz*R_wire^2;
        end
        for j=2:j_max-1
            m(i,j)=p_wire*pi*dz*R_wire^2;
        end
        for j=j_max
            m(i,j)=.5*p_wire*pi*dz*R_wire^2;
        end
    end
    % Side Wall Mass
    for i=i_max
        for j=1
            m(i,j)=.5*p_prop*pi*dz*(r(i)^2-(r(i)-dr/2)^2);
        end
        for j=2:j_max-1
            m(i,j)=p_prop*pi*dz*(r(i)^2-(r(i)-dr/2)^2);
        end
        for j=j_max
            m(i,j)=.5*p_prop*pi*dz*(r(i)^2-(r(i)-dr/2)^2);
        end
    end
% Mass of Propellant along Wire
    for i=2
        for j=1
            m(i,j)=.5*p_prop*pi*dz*((r(i)+dr/2)^2-R_wire^2);
        end
        for j=2:j_max-1
            m(i,j)=p_prop*pi*dz*((r(i)+dr/2)^2-R_wire^2);
        end
        for j=j_max
            m(i,j)=.5*p_prop*pi*dz*((r(i)+dr/2)^2-R_wire^2);
        end
    end
% Internal Mass
    for i=3:i_max-1
        for j=1
            m(i,j)=.5*p_prop*pi*dz*((r(i)+dr/2)^2-(r(i)-dr/2)^2);
        end
        for j=2:j_max-1
            m(i,j)=p_prop*pi*dz*((r(i)+dr/2)^2-(r(i)-dr/2)^2);
```

```
        end
        for j=j_max
            m(i,j)=.5*p_prop*pi*dz*((r(i)+dr/2)^2-(r(i)-dr/2)^2);
        end
    end
% Initial Total Mass of Propellant (Wire mass not included)
    Total_mass=0;
    for i=2:i_max
        for j=1:j_max
            Total_mass=Total_mass+m(i,j);
        end
    end
end
end
```

## Appendix C: Mass Function

```
% new_mass.m
% Updates mass of each cell by computing a new burn rate and burn distance
% for each time step and reduces the mass of boundary cells accordingly.

function
[m,burn_distance,Total_Mass_Left,br,br_r,m_gen,m_dot_gen,burn_distancen,burn_di
stancen_r] =
new_mass(Wire,MultiWire,m,i_max,j_max,dz,dr,br,dt,T,P_c,burn_distance,burn_dist
ancen,burn_distance_r,burn_distancen_r,m_int,br_r,p_prop,r,z,T_melt,R_wire,R_ca
se,R_max)

if Wire==0
    rate=3.212E-4*exp(1.84E-3*(252-288))*((4E6)^.21);
% Starting Mass for Current Time step
    Total_Mass_Start=0;
    for i=1:i_max
        for j=1:j_max
            Total_Mass_Start=Total_Mass_Start+m(i,j);
        end
    end
% Burn Rate Calculations
    for i=1:i_max
        for j=1
            br(i,j)=rate;
            if m(i,j)==0
                br(i,j)=0;
            end
        end
        for j=2:j_max
            if m(i,j)==0
                br(i,j)=0;
            elseif m(i,j-1)==0 && m(i,j)>0
                br(i,j)=rate;
            end
        end
    end
% Burn Distance Calculations
    for i=1:i_max
        for j=1:j_max
            burn_distance(i,j)=br(i,j)*dt;
        end
    end
    burn_distance=burn_distance+burn_distancen;
    for i=1:i_max
        for j=1
            if burn_distance(i,j)<=dz/2
```

```
                m(i,j)=(1-(burn_distance(i,j)/(dz/2)))*m_int(i,j);
            elseif burn_distance(i,j)>dz/2 && m(i,j+1)==m_int(i,j+1)
                m(i,j)=0;
                burn_distance(i,j+1)=burn_distance(i,j)-dz/2;
                burn_distance(i,j)=dz/2;
            else
                m(i,j)=0;
            end
        end
        for j=2:j_max-1
            if burn_distance(i,j)<=dz
                m(i,j)=(1-burn_distance(i,j)/dz)*m_int(i,j);
            elseif burn_distance(i,j)>dz && m(i,j+1)==m_int(i,j+1)
                m(i,j)=0;
                burn_distance(i,j+1)=burn_distance(i,j)-dz;
                burn_distance(i,j)=dz;
            else
                m(i,j)=0;
            end
        end
        for j=j_max
            if burn_distance(i,j)<=dz/2
                m(i,j)=(1-(burn_distance(i,j)/(dz/2)))*m_int(i,j);
            elseif burn_distance(i,j)>dz/2
                m(i,j)=0;
            end
        end
    end
    burn_distancen=burn_distance;
% Mass Left after time step
    Total_Mass_Left=0;
    for i=1:i_max
        for j=1:j_max
            Total_Mass_Left=Total_Mass_Left+m(i,j);
        end
    end
% Mass Generated
    m_gen=Total_Mass_Start-Total_Mass_Left;
    m_dot_gen=(Total_Mass_Start-Total_Mass_Left)/dt;

elseif Wire==1
    ao=3.212E-4;
    sigma_p=.00184;
    n_n=.21;
% Adjusting wire mass for temperature
    for i=1
        for j=1:j_max
            if T(i,j)>=T_melt
```

```
                m(i,j)=0;
            else
                m(i,j)=m(i,j);
            end
        end
    end
% Starting Mass for Current Time step
    Total_Mass_Start=0;
    for i=2:i_max
        for j=1:j_max
            Total_Mass_Start=Total_Mass_Start+m(i,j);
        end
    end
% Burn Rate Calculations
    for i=2:i_max
        for j=1
            br(i,j)=ao*exp(sigma_p*(T(i,j)-288))*P_c^n_n;
            if m(i,j)==0
                br(i,j)=0;
                br_r(i,j)=0;
            end
            if m(i-1,j)==0 && m(i,j)>0
                br_r(i,j)=ao*exp(sigma_p*(T(i,j)-288))*P_c^n_n;
            end
        end
        for j=2:j_max
            if m(i,j)==0
                br(i,j)=0;
                br_r(i,j)=0;
            elseif m(i,j-1)==0 && m(i-1,j)>0
                br(i,j)=ao*exp(sigma_p*(T(i,j)-288))*P_c^n_n;
                br_r(i,j)=0;
            elseif m(i,j-1)==0 && m(i-1,j)==0
                br(i,j)=ao*exp(sigma_p*(T(i,j)-288))*P_c^n_n;
                br_r(i,j)=ao*exp(sigma_p*(T(i,j)-288))*P_c^n_n;
            elseif m(i,j-1)>0 && m(i-1,j)==0
                br(i,j)=0;
                br_r(i,j)=ao*exp(sigma_p*(T(i,j)-288))*P_c^n_n;
            end
        end
    end
% Burn Distance Calculations
    for i=2:i_max
        for j=1:j_max
            burn_distance(i,j)=br(i,j)*dt;
            burn_distance_r(i,j)=br_r(i,j)*dt;
        end
    end
```

```
    burn_distance=burn_distance+burn_distancen;
    burn_distance_r=burn_distance_r+burn_distancen_r;
    for i=2
        for j=1
            if burn_distance(i,j)<=dz/2 && burn_distance_r(i,j)<=(r(i)+dr/2-
R_wire)
                m(i,j)=p_prop*pi*((r(i)+dr/2)^2-
(R_wire+burn_distance_r(i,j))^2)*((dz/2)-burn_distance(i,j));
            elseif burn_distance(i,j)>dz/2 && m(i,j+1)==m_int(i,j+1)
                m(i,j)=0;
                burn_distance(i,j+1)=burn_distance(i,j)-dz/2;
                burn_distance(i,j)=dz/2;
            elseif burn_distance_r(i,j)>(r(i)+dr/2-R_wire) &&
m(i+1,j)==m_int(i+1,j)
                m(i,j)=0;
                burn_distance_r(i+1,j)=burn_distance_r(i,j)-(r(i)+dr/2-R_wire);
                burn_distance_r(i,j)=(r(i)+dr/2-R_wire);
            else
                m(i,j)=0;
            end
        end
        for j=2:j_max-1
            if burn_distance(i,j)<=dz && burn_distance_r(i,j)<=(r(i)+dr/2-
R_wire)
                m(i,j)=p_prop*pi*((r(i)+dr/2)^2-
(R_wire+burn_distance_r(i,j))^2)*(dz-burn_distance(i,j));
            elseif burn_distance(i,j)>dz && m(i,j+1)==m_int(i,j+1)
                m(i,j)=0;
                burn_distance(i,j+1)=burn_distance(i,j)-dz;
                burn_distance(i,j)=dz;
            elseif burn_distance_r(i,j)>(r(i)+dr/2-R_wire) &&
m(i+1,j)==m_int(i+1,j)
                m(i,j)=0;
                burn_distance_r(i+1,j)=burn_distance_r(i,j)-(r(i)+dr/2-R_wire);
                burn_distance_r(i,j)=(r(i)+dr/2-R_wire);
            else
                m(i,j)=0;
            end
        end
        for j=j_max
            if burn_distance(i,j)<=dz/2 && burn_distance_r(i,j)<=(r(i)+dr/2-
R_wire)
                m(i,j)=p_prop*pi*((r(i)+dr/2)^2-
(R_wire+burn_distance_r(i,j))^2)*((dz/2)-burn_distance(i,j));
            elseif burn_distance(i,j)>dz/2 || burn_distance_r(i,j)>(r(i)+dr/2-
R_wire)
                m(i,j)=0;
            end
```

```
        end
    end
    for i=3:i_max-1
        for j=1
            if burn_distance(i,j)<=dz/2 && burn_distance_r(i,j)<=dr
                m(i,j)=p_prop*pi*((r(i)+dr/2)^2-(r(i)-
(dr/2)+burn_distance_r(i,j))^2)*((dz/2)-burn_distance(i,j));
            elseif burn_distance(i,j)>dz/2 && m(i,j+1)==m_int(i,j+1)
                m(i,j)=0;
                burn_distance(i,j+1)=burn_distance(i,j)-dz/2;
                burn_distance(i,j)=dz/2;
            elseif burn_distance_r(i,j)>dr && m(i+1,j)==m_int(i+1,j)
                m(i,j)=0;
                burn_distance_r(i+1,j)=burn_distance_r(i,j)-dr;
                burn_distance_r(i,j)=dr;
            else
                m(i,j)=0;
            end
        end
        for j=2:j_max-1
            if burn_distance(i,j)<=dz && burn_distance_r(i,j)<=dr
                m(i,j)=p_prop*pi*((r(i)+dr/2)^2-(r(i)-
(dr/2)+burn_distance_r(i,j))^2)*(dz-burn_distance(i,j));
            elseif burn_distance(i,j)>dz && m(i,j+1)==m_int(i,j+1)
                m(i,j)=0;
                burn_distance(i,j+1)=burn_distance(i,j)-dz;
                burn_distance(i,j)=dz;
            elseif burn_distance_r(i,j)>dr && m(i+1,j)==m_int(i+1,j)
                m(i,j)=0;
                burn_distance_r(i+1,j)=burn_distance_r(i,j)-dr;
                burn_distance_r(i,j)=dr;
            else
                m(i,j)=0;
            end
        end
        for j=j_max
            if burn_distance(i,j)<=dz/2 && burn_distance_r(i,j)<=dr
                m(i,j)=p_prop*pi*((r(i)+dr/2)^2-(r(i)-
(dr/2)+burn_distance_r(i,j))^2)*((dz/2)-burn_distance(i,j));
            elseif burn_distance(i,j)>dz/2 || burn_distance_r(i,j)>dr
                m(i,j)=0;
            end
        end
    end
    for i=i_max
        for j=1
            if burn_distance(i,j)<=dz/2 && burn_distance_r(i,j)<=dr/2
                m(i,j)=p_prop*pi*((r(i))^2-(r(i)-
(dr/2)+burn_distance_r(i,j))^2)*((dz/2)-burn_distance(i,j));
```

```
            elseif burn_distance(i,j)>dz/2 && m(i,j+1)==m_int(i,j+1)
                m(i,j)=0;
                burn_distance(i,j+1)=burn_distance(i,j)-dz/2;
                burn_distance(i,j)=dz/2;
            elseif burn_distance_r(i,j)>dr && m(i+1,j)==m_int(i+1,j)
                m(i,j)=0;
                burn_distance_r(i+1,j)=burn_distance_r(i,j)-dr/2;
                burn_distance_r(i,j)=dr/2;
            else
                m(i,j)=0;
            end
        end
        for j=2:j_max-1
            if burn_distance(i,j)<=dz && burn_distance_r(i,j)<=dr/2
                m(i,j)=p_prop*pi*((r(i))^2-(r(i)-
(dr/2)+burn_distance_r(i,j))^2)*(dz-burn_distance(i,j));
            elseif burn_distance(i,j)>dz && m(i,j+1)==m_int(i,j+1)
                m(i,j)=0;
                burn_distance(i,j+1)=burn_distance(i,j)-dz;
                burn_distance(i,j)=dz;
            elseif burn_distance_r(i,j)>dr && m(i+1,j)==m_int(i+1,j)
                m(i,j)=0;
                burn_distance_r(i+1,j)=burn_distance_r(i,j)-dr/2;
                burn_distance_r(i,j)=dr/2;
            else
                m(i,j)=0;
            end
        end
        for j=j_max
            if burn_distance(i,j)<=dz/2 && burn_distance_r(i,j)<=dr/2
                m(i,j)=p_prop*pi*((r(i))^2-(r(i)-
(dr/2)+burn_distance_r(i,j))^2)*((dz/2)-burn_distance(i,j));
            elseif burn_distance(i,j)>dz/2 || burn_distance_r(i,j)>dr/2
                m(i,j)=0;
            end
        end
    end
    burn_distancen=burn_distance;
    burn_distancen_r=burn_distance_r;
% Mass Left after time step
    Total_Mass_Left=0;
    for i=2:i_max
        for j=1:j_max
            Total_Mass_Left=Total_Mass_Left+m(i,j);
        end
    end
    if MultiWire>0
        Total_Mass_Start=MultiWire*Total_Mass_Start;
        Total_Mass_Left=MultiWire*Total_Mass_Left;
```

```
% Mass Generated
        if Total_Mass_Left==0
            m_gen=Total_Mass_Start-Total_Mass_Left;
            m_dot_gen=(Total_Mass_Start-Total_Mass_Left)/dt;
        else
            if br_r(i_max,:)==0
                br_ave=.0091;
                A_ave=(pi*R_case^2-MultiWire*pi*R_max^2);
                m_gen=Total_Mass_Start-Total_Mass_Left+A_ave*br_ave*dt*p_prop;
                m_dot_gen=(Total_Mass_Start-Total_Mass_Left)/dt;
            else
                br_ave=sqrt(.0091^2+.0091^2);  %Propellant Specific, magnitude
of average burn rate in axial and radial direction
                %A_ave=(pi*R_case^2-MultiWire*pi*R_max^2)/(cos(atan(32/4))); %
CNT
                A_ave=(pi*R_case^2-MultiWire*pi*R_max^2)/(cos(atan(15/8))); %
Silver
                m_gen=Total_Mass_Start-Total_Mass_Left+A_ave*br_ave*dt*p_prop;
                m_dot_gen=(Total_Mass_Start-Total_Mass_Left)/dt;
            end
        end
    elseif MultiWire==0
% Mass Generated
        m_gen=Total_Mass_Start-Total_Mass_Left;
        m_dot_gen=(Total_Mass_Start-Total_Mass_Left)/dt;
    end
end
end
```

# Appendix D: Temperature Function

```
% new_mass.m
% Updates mass of each cell by computing a new burn rate and burn distance
% for each time step and reduces the mass of boundary cells accordingly.

function
[m,burn_distance,Total_Mass_Left,br,br_r,m_gen,m_dot_gen,burn_distancen,burn_di
stancen_r] =
new_mass(Wire,MultiWire,m,i_max,j_max,dz,dr,br,dt,T,P_c,burn_distance,burn_dist
ancen,burn_distance_r,burn_distancen_r,m_int,br_r,p_prop,r,T_melt,R_wire,R_case
,R_max)

if Wire==0
    rate=3.212E-4*exp(1.84E-3*(252-288))*((4E6)^.21);
% Starting Mass for Current Time step
    Total_Mass_Start=0;
    for i=1:i_max
        for j=1:j_max
            Total_Mass_Start=Total_Mass_Start+m(i,j);
        end
    end
% Burn Rate Calculations
    for i=1:i_max
        for j=1
            br(i,j)=rate;
            if m(i,j)==0
                br(i,j)=0;
            end
        end
        for j=2:j_max
            if m(i,j)==0
                br(i,j)=0;
            elseif m(i,j-1)==0 && m(i,j)>0
                br(i,j)=rate;
            end
        end
    end
% Burn Distance Calculations
    for i=1:i_max
        for j=1:j_max
            burn_distance(i,j)=br(i,j)*dt;
        end
    end
    burn_distance=burn_distance+burn_distancen;
    for i=1:i_max
        for j=1
            if burn_distance(i,j)<=dz/2
```

```
                m(i,j)=(1-(burn_distance(i,j)/(dz/2)))*m_int(i,j);
            elseif burn_distance(i,j)>dz/2 && m(i,j+1)==m_int(i,j+1)
                m(i,j)=0;
                burn_distance(i,j+1)=burn_distance(i,j)-dz/2;
                burn_distance(i,j)=dz/2;
            else
                m(i,j)=0;
            end
        end
        for j=2:j_max-1
            if burn_distance(i,j)<=dz
                m(i,j)=(1-burn_distance(i,j)/dz)*m_int(i,j);
            elseif burn_distance(i,j)>dz && m(i,j+1)==m_int(i,j+1)
                m(i,j)=0;
                burn_distance(i,j+1)=burn_distance(i,j)-dz;
                burn_distance(i,j)=dz;
            else
                m(i,j)=0;
            end
        end
        for j=j_max
            if burn_distance(i,j)<=dz/2
                m(i,j)=(1-(burn_distance(i,j)/(dz/2)))*m_int(i,j);
            elseif burn_distance(i,j)>dz/2
                m(i,j)=0;
            end
        end
    end
    burn_distancen=burn_distance;
% Mass Left after time step
    Total_Mass_Left=0;
    for i=1:i_max
        for j=1:j_max
            Total_Mass_Left=Total_Mass_Left+m(i,j);
        end
    end
% Mass Generated
    m_gen=Total_Mass_Start-Total_Mass_Left;
    m_dot_gen=(Total_Mass_Start-Total_Mass_Left)/dt;

elseif Wire==1
    ao=3.212E-4;
    sigma_p=.00184;
    n_n=.21;
% Adjusting wire mass for temperature
    for i=1
        for j=1:j_max
            if T(i,j)>=T_melt
```

```
                m(i,j)=0;
            else
                m(i,j)=m(i,j);
            end
        end
    end
% Starting Mass for Current Time step
    Total_Mass_Start=0;
    for i=2:i_max
        for j=1:j_max
            Total_Mass_Start=Total_Mass_Start+m(i,j);
        end
    end
% Burn Rate Calculations
    for i=2:i_max
        for j=1
            br(i,j)=ao*exp(sigma_p*(T(i,j)-288))*P_c^n_n;
            if m(i,j)==0
                br(i,j)=0;
                br_r(i,j)=0;
            end
            if m(i-1,j)==0 && m(i,j)>0
                br_r(i,j)=ao*exp(sigma_p*(T(i,j)-288))*P_c^n_n;
            end
        end
        for j=2:j_max
            if m(i,j)==0
                br(i,j)=0;
                br_r(i,j)=0;
            elseif m(i,j-1)==0 && m(i-1,j)>0
                br(i,j)=ao*exp(sigma_p*(T(i,j)-288))*P_c^n_n;
                br_r(i,j)=0;
            elseif m(i,j-1)==0 && m(i-1,j)==0
                br(i,j)=ao*exp(sigma_p*(T(i,j)-288))*P_c^n_n;
                br_r(i,j)=ao*exp(sigma_p*(T(i,j)-288))*P_c^n_n;
            elseif m(i,j-1)>0 && m(i-1,j)==0
                br(i,j)=0;
                br_r(i,j)=ao*exp(sigma_p*(T(i,j)-288))*P_c^n_n;
            end
        end
    end
% Burn Distance Calculations
    for i=2:i_max
        for j=1:j_max
            burn_distance(i,j)=br(i,j)*dt;
            burn_distance_r(i,j)=br_r(i,j)*dt;
        end
    end
```

```
    burn_distance=burn_distance+burn_distancen;
    burn_distance_r=burn_distance_r+burn_distancen_r;
    for i=2
        for j=1
            if burn_distance(i,j)<=dz/2 && burn_distance_r(i,j)<=(r(i)+dr/2-
R_wire)
                m(i,j)=p_prop*pi*((r(i)+dr/2)^2-
(R_wire+burn_distance_r(i,j))^2)*((dz/2)-burn_distance(i,j));
            elseif burn_distance(i,j)>dz/2 && m(i,j+1)==m_int(i,j+1)
                m(i,j)=0;
                burn_distance(i,j+1)=burn_distance(i,j)-dz/2;
                burn_distance(i,j)=dz/2;
            elseif burn_distance_r(i,j)>(r(i)+dr/2-R_wire) &&
m(i+1,j)==m_int(i+1,j)
                m(i,j)=0;
                burn_distance_r(i+1,j)=burn_distance_r(i,j)-(r(i)+dr/2-R_wire);
                burn_distance_r(i,j)=(r(i)+dr/2-R_wire);
            else
                m(i,j)=0;
            end
        end
        for j=2:j_max-1
            if burn_distance(i,j)<=dz && burn_distance_r(i,j)<=(r(i)+dr/2-
R_wire)
                m(i,j)=p_prop*pi*((r(i)+dr/2)^2-
(R_wire+burn_distance_r(i,j))^2)*(dz-burn_distance(i,j));
            elseif burn_distance(i,j)>dz && m(i,j+1)==m_int(i,j+1)
                m(i,j)=0;
                burn_distance(i,j+1)=burn_distance(i,j)-dz;
                burn_distance(i,j)=dz;
            elseif burn_distance_r(i,j)>(r(i)+dr/2-R_wire) &&
m(i+1,j)==m_int(i+1,j)
                m(i,j)=0;
                burn_distance_r(i+1,j)=burn_distance_r(i,j)-(r(i)+dr/2-R_wire);
                burn_distance_r(i,j)=(r(i)+dr/2-R_wire);
            else
                m(i,j)=0;
            end
        end
        for j=j_max
            if burn_distance(i,j)<=dz/2 && burn_distance_r(i,j)<=(r(i)+dr/2-
R_wire)
                m(i,j)=p_prop*pi*((r(i)+dr/2)^2-
(R_wire+burn_distance_r(i,j))^2)*((dz/2)-burn_distance(i,j));
            elseif burn_distance(i,j)>dz/2 || burn_distance_r(i,j)>(r(i)+dr/2-
R_wire)
                m(i,j)=0;
            end
```

```
        end
    end
    for i=3:i_max-1
        for j=1
            if burn_distance(i,j)<=dz/2 && burn_distance_r(i,j)<=dr
                m(i,j)=p_prop*pi*((r(i)+dr/2)^2-(r(i)-
(dr/2)+burn_distance_r(i,j))^2)*((dz/2)-burn_distance(i,j));
            elseif burn_distance(i,j)>dz/2 && m(i,j+1)==m_int(i,j+1)
                m(i,j)=0;
                burn_distance(i,j+1)=burn_distance(i,j)-dz/2;
                burn_distance(i,j)=dz/2;
            elseif burn_distance_r(i,j)>dr && m(i+1,j)==m_int(i+1,j)
                m(i,j)=0;
                burn_distance_r(i+1,j)=burn_distance_r(i,j)-dr;
                burn_distance_r(i,j)=dr;
            else
                m(i,j)=0;
            end
        end
        for j=2:j_max-1
            if burn_distance(i,j)<=dz && burn_distance_r(i,j)<=dr
                m(i,j)=p_prop*pi*((r(i)+dr/2)^2-(r(i)-
(dr/2)+burn_distance_r(i,j))^2)*(dz-burn_distance(i,j));
            elseif burn_distance(i,j)>dz && m(i,j+1)==m_int(i,j+1)
                m(i,j)=0;
                burn_distance(i,j+1)=burn_distance(i,j)-dz;
                burn_distance(i,j)=dz;
            elseif burn_distance_r(i,j)>dr && m(i+1,j)==m_int(i+1,j)
                m(i,j)=0;
                burn_distance_r(i+1,j)=burn_distance_r(i,j)-dr;
                burn_distance_r(i,j)=dr;
            else
                m(i,j)=0;
            end
        end
        for j=j_max
            if burn_distance(i,j)<=dz/2 && burn_distance_r(i,j)<=dr
                m(i,j)=p_prop*pi*((r(i)+dr/2)^2-(r(i)-
(dr/2)+burn_distance_r(i,j))^2)*((dz/2)-burn_distance(i,j));
            elseif burn_distance(i,j)>dz/2 || burn_distance_r(i,j)>dr
                m(i,j)=0;
            end
        end
    end
    for i=i_max
        for j=1
            if burn_distance(i,j)<=dz/2 && burn_distance_r(i,j)<=dr/2
                m(i,j)=p_prop*pi*((r(i))^2-(r(i)-
(dr/2)+burn_distance_r(i,j))^2)*((dz/2)-burn_distance(i,j));
```

```
            elseif burn_distance(i,j)>dz/2 && m(i,j+1)==m_int(i,j+1)
                m(i,j)=0;
                burn_distance(i,j+1)=burn_distance(i,j)-dz/2;
                burn_distance(i,j)=dz/2;
            elseif burn_distance_r(i,j)>dr && m(i+1,j)==m_int(i+1,j)
                m(i,j)=0;
                burn_distance_r(i+1,j)=burn_distance_r(i,j)-dr/2;
                burn_distance_r(i,j)=dr/2;
            else
                m(i,j)=0;
            end
        end
        for j=2:j_max-1
            if burn_distance(i,j)<=dz && burn_distance_r(i,j)<=dr/2
                m(i,j)=p_prop*pi*((r(i))^2-(r(i)-
(dr/2)+burn_distance_r(i,j))^2)*(dz-burn_distance(i,j));
            elseif burn_distance(i,j)>dz && m(i,j+1)==m_int(i,j+1)
                m(i,j)=0;
                burn_distance(i,j+1)=burn_distance(i,j)-dz;
                burn_distance(i,j)=dz;
            elseif burn_distance_r(i,j)>dr && m(i+1,j)==m_int(i+1,j)
                m(i,j)=0;
                burn_distance_r(i+1,j)=burn_distance_r(i,j)-dr/2;
                burn_distance_r(i,j)=dr/2;
            else
                m(i,j)=0;
            end
        end
        for j=j_max
            if burn_distance(i,j)<=dz/2 && burn_distance_r(i,j)<=dr/2
                m(i,j)=p_prop*pi*((r(i))^2-(r(i)-
(dr/2)+burn_distance_r(i,j))^2)*((dz/2)-burn_distance(i,j));
            elseif burn_distance(i,j)>dz/2 || burn_distance_r(i,j)>dr/2
                m(i,j)=0;
            end
        end
    end
    burn_distancen=burn_distance;
    burn_distancen_r=burn_distance_r;
% Mass Left after time step
    Total_Mass_Left=0;
    for i=2:i_max
        for j=1:j_max
            Total_Mass_Left=Total_Mass_Left+m(i,j);
        end
    end
    if MultiWire>0
        Total_Mass_Start=MultiWire*Total_Mass_Start;
        Total_Mass_Left=MultiWire*Total_Mass_Left;
```

```
% Mass Generated
        if Total_Mass_Left==0
            m_gen=Total_Mass_Start-Total_Mass_Left;
            m_dot_gen=(Total_Mass_Start-Total_Mass_Left)/dt;
        else
        m_gen=Total_Mass_Start-Total_Mass_Left+5*(pi*R_case^2-
MultiWire*pi*R_max^2)*.012*dt*p_prop;
        m_dot_gen=(Total_Mass_Start-Total_Mass_Left)/dt;
        end
    elseif MultiWire==0
% Mass Generated
        m_gen=Total_Mass_Start-Total_Mass_Left;
        m_dot_gen=(Total_Mass_Start-Total_Mass_Left)/dt;
    end
end
end
```

# Appendix E: Chamber Function

```
% chamber_Final.m
% Computes chamber and exit conditions at each time step and feeds it back
% into the main script.

function [m_dot_out,P_c,m_c,V_c,v_exit,F,P_2] =
Chamber(m_c,m_gen,A_t,gamma,R,T_comb,V_c,p_prop,dt,P_2,P_amb,A_2,P_c,P2_Pc)
% Isentropic Flow
% Chamber Conditions
m_dot_out=A_t*P_c*gamma*sqrt((2/(gamma+1))^((gamma+1)/(gamma-
1)))/sqrt(gamma*R*T_comb);
m_out=m_dot_out*dt;
v_exit=sqrt(((2*gamma)/(gamma-1))*R*T_comb*(1-(P2_Pc)^((gamma-1)/gamma)));
F=m_dot_out*v_exit+(P_2-P_amb)*A_2;
m_c=m_c+m_gen-m_out;
V_c=V_c+m_gen/p_prop;
P_c=(m_c/V_c)*R*T_comb;
P_2=P2_Pc*P_c;
end
```

# Appendix F: Star Grain

```
% Code is modified from Grain_Design_III.m by Maj Carl Hartsfield,
% September 2003, AA4452

%Script file to generate values of Burning Area as a function of burn back
%distance for a star geometry of fixed parameters, including burn rate and
%burn time.

clear all; clc;
% Geometric Parameters
L = 600; %mm, Length of Motor
R = 80; % mm, Radius of Motor
%tb = 5.4795; % sec, burn time
tb = 4.0011; % sec, burn time
rdot = 7.3; % mm/s, burn rate
N =5; % number of star points
% Calculated Quantities
w = tb*rdot; % Web thickness
wf = w/R;
phi = pi/N;
functionstring = '-tan(pi/2-x)+pi/2-x';
functionstring = [num2str(phi), functionstring];
eta = fzero(functionstring,0.5); % Find value of eta
xi = phi;
product1 = wf/(1-wf)*cos(eta); %
if abs(product1)<=sin(xi)
    xi = asin(wf/(1-wf)*cos(eta)); % Value of xi for no progressive region III
else
    xi = phi;
end
%xi=phi;
alpha = 0.5*pi-eta+xi;
% Loop over burn in distance, wx
dwx = w/4000;Athree = 1;
x1 = eta;
for bd = 1:4000
    wx = bd*dwx;
    H = (R-w+wx);
    if wx<=w
        Aone = (R-w+wx)*(phi-xi);
        Atwo = (0+wx)*alpha;
        Athree = (R-w)*(sin(xi)/sin(eta))-(0+wx)*tan(pi/2-eta);
        Ab(bd) = (Aone>0)*Aone+(Atwo>0)*Atwo+(Athree>0)*Athree;
    else
        rs = num2str(R);
        ws = num2str(w);
        wxs = num2str(wx);
```

```
        xis = num2str(xi);
        functionstring = [rs,'-sqrt(((' rs '-' ws ')*sin(' xis ')+' wxs
'*sin(x))^2+((' rs '-' ws ')*cos(' xis ')+' wxs '*cos(x))^2)'];
        x = fzero(functionstring,-.3);
        y = -asin((R-w)*sin(xi)/wx);
        zeta = alpha*(alpha<(x-y))+(x-y)*(alpha>x-y);
        Ab(bd)=wx*(x-y)*((x-y)>0);
    end
    WX(bd) = wx;
end
volburned(1) = 0;
for bd = 1:3999
    volburned(bd+1)= L*dwx*0.5*(Ab(bd+1)+Ab(bd));
end
WX=WX*.001;
Ab = 2*N*Ab*L*.001^2;
volburned = 2*N*volburned*.001^3;
limit = (Ab(5)*0.95)*ones(size(Ab));
index = length(find(Ab>limit));
volburned(index);
vtotal = R^2*pi*L*.001^3;
Vfuseful = sum(volburned(1:index))/vtotal;
Vfill=sum(volburned)/vtotal;
for bd = 1:4000
    Ap(4001-bd) = (vtotal-volburned(bd))/(L);
end
p_prop=1760.44;
Total_mass=sum(volburned)*p_prop;
Used_mass=sum(volburned(1:index))*p_prop;
m_g=volburned*p_prop;
time=linspace(0,tb,4000);
g=9.8066;
T_comb=3472;
P_c=4E6;
P_2=50539;
P_amb=P_2;
P2_Pc=P_2/P_c;
gamma=1.17;
R=283.77;
A_2=pi*(.08)^2;
A_t=((A_2*16*.0073*p_prop)/(P_c))*sqrt((R*T_comb)/(gamma*(2/(gamma+1))^((gamma+
1)/(gamma-1))));
r_t=sqrt(A_t/pi);
h=.1;
V_c=(pi*h/12)*((2*.08)^2+4*.08*r_t+(2*r_t)^2)+vtotal-sum(volburned);
m_c=P_c*V_c/(R*T_comb);
dt=tb/4000;
```

```
m_g=[m_g(1:index) zeros(1,1000)];
count=linspace(index,index+1000,1000);
time=[time(1:index) dt*count];
iter=index+1000;
Exit_Velocity=zeros(1,iter-1);
Mdot_v=zeros(1,iter-1);
Pressure=zeros(1,iter-1);
Thrust=zeros(1,iter-1);

for k=2:iter
    m_gen=m_g(k);

[m_dot_out,P_c,m_c,V_c,v_exit,F,P_2]=chamber_Final(m_c,m_gen,A_t,gamma,R,T_comb
,V_c,p_prop,dt,P_2,P_amb,A_2,P_c,P2_Pc);
    Exit_Velocity(k)=v_exit;
    Mdot_v(k)=m_dot_out;
    Pressure(k)=P_c;
    Thrust(k)=F;
end
indices=find(Thrust>=0);
It=sum(dt*Thrust(1:indices(end)));
Isp=It/(g*Used_mass);
indices = find((Pressure-.1*max(Pressure))>=0);
ave_Pressure=sum(Pressure(indices(1):indices(end)))/length(Pressure(indices(1):
indices(end)));
indices = find((Thrust-.1*max(Thrust))>=0);
ave_Thrust=sum(Thrust(indices(1):indices(end)))/length(Thrust(indices(1):indice
s(end)));
max_Thrust=max(Thrust);
max_Pressure=max(Pressure);
```

# Bibliography

[1] G. Sutton and O. Biblarz, Rocket Propulsion Elements 9th Edition, Hoboken, New Jersey: John Wiley & Sons, Inc, 2016.

[2] "Solid Propellant Grain Design and Internal Ballistics," NASA SP-8076, 1972.

[3] A. Davenas, "Solid Rocket Motor Design," in *Tactical Missile Propulsion*, Reston, VA, American Institute of Aeronautics and A, 1996, pp. 57-113.

[4] "Solid Propellant Selection and Characterization," NASA SP-8064, 1971.

[5] G. E. Jensen, D. W. Netzer and P. Zarchan, "Tactical Missile Propulsion," *Progress in Astronautics and Aeronautics,* vol. 170, 1996.

[6] T. Bergman, D. DeWitt, F. Incropera and A. and Lavine, Fundamentals of Heat and Mass Transfer Seventh Edition, Hoboken, New Jersey: John Wiley & Sons, Inc., 2011.

[7] L. Caveny and R. Glick, "Influence of Embedded Metal Fibers on Solid-Propellant Burning Rate," *Journal of Spacecraft and Rockets,* vol. 4, no. 1, pp. 79-85, 1967.

[8] M. King, "Analytical Modeling of Effects of Wires on SOlid Motor Ballistics," *Journal of Propulsion and Power,* vol. 7, no. 3, pp. 312-321, 1991.

[9] D. Smith, "A Comparison of Experimental Heat-Transfer Coefficients in a Nozzle with Analytical Predictions from Bartz's Methods for Various Combustion Chamber Pressures in a Solid Propllant Rocket Motors," Thesis, 1969, 1969.

[10] D. A. Anderson, R. H. Pletcher and J. C. Tannehill, Computational Fluid Mechanics and Heat Transfer Third Edition, Taylor & Francis Group, LLC, 2013.

[11] R. D. Richtmyer and K. W. Morton, Difference Methods for Initial-Value Problems, Krieger Publishing, 1994.

[12] W. S. McEwan, A. S. Gordon and J. Cohen, "Method for Increasing the Burning Rate of Propellants". US Patent 3,228,338, 11 January 1966.

[13] K. E. Rumbel and M. Cohen, "Propellent Grains". US Patent 3,109,375, 1963.

[14] K. E. Rumbel and M. Cohen, "Propellent Grains". US Patent 3,109,374, 1963.

[15] K. E. Rumbel, M. Cohen, R. G. Nugent and A. C. Scurlock, "Propellent Grains". US Patent 3,116,692, 1964.

[16] N. Kubota, M. Ichidaf and T. Fujisawat, "Combustion Processes of Propellants with Embedded Metal Wires," *AIAA Journal,* vol. 20, no. 1, pp. 116-121, 1982.

[17] A. Davenas, "Development of Modern Solid Propellants," *Journal Of Propulsion and Power,* vol. 19, no. 6, pp. 1108-1125, 2003.

[18] T. Goodman, "Applications of Integral Methods to Transient Nonlinear Heat Transfer," *Advances in Heat Transfer,* vol. 1, pp. 51-122, 1964.

[19] T. J. Lardner and F. V. Pohle, "Applications of the Heat Balance Integral to Problems of Cylindrical Geometry," *Transactions of the ASME Journal of Applied Mechanics,* vol. 28, no. 2, p. 310, 1961.

[20] (FOUO) 2012 Weapons File, Eglin AFB, Florida: Life Cycle Management Center, 2012.

[21] N. Hall, "Nose Cone Volume," NASA Glenn Research Center, 5 May 2015. [Online]. Available: https://www.grc.nasa.gov/www/k-12/airplane/volume.html. [Accessed December 2018].

[22] W. Cai, P. Thakre and V. Yang, "A Model of AP/HTPB Composite Propellant Combustion in Rocket-motor Environments," *Combustion Science and Technology,* 2008.

[23] J. Buckmaster, T. Jackson and X. and Wang, "Modelling of Propellants containing Ultrafine Aluminum," *Journal of Propulsion and Power,* vol. 23, no. 1, pp. 158-165, 2007.

[24] H. Duan, G. Iannacchione, J. Liang and N. Pradhan, "The Specific Heat and Effective Thermal Conductivity of Composites containing Single-Wall and Multi-Wall Carbon Nanotubes," *Nanotechnology,* 2009.

[25] K. Zhang, M. G. Stocks and J. Zhong, "Metling and Premelting of Carbon Nanotubes," *Nanotechnology,* vol. 18, no. 28, 2007.

[26] L. Dombrovsky, "Emissivity of Two-Phase Combustion Products in a Solid-Propellant Rocket Engine," Thermopedia, 7 September 2010. [Online]. Available: http://www.thermopedia.com/content/179/. [Accessed January 2019].

| REPORT DOCUMENTATION PAGE | *Form Approved*<br>*OMB No. 074-0188* |
|---|---|

| **1. REPORT DATE** *(DD-MM-YYYY)* | **2. REPORT TYPE** | **3. DATES COVERED** *(From – To)* |
|---|---|---|
| 21-03-2019 | Master's Thesis | September 2017 – March 2019 |

| **TITLE AND SUBTITLE** | |
|---|---|
| TACTICAL MISSILE PERFORMANCE FOR SINGLE AND MULTI-WIRE EMBEDDED PROPELLANT CONFIGURATIONS WITH DISCONTINUITIES | **5a. CONTRACT NUMBER**<br>**5b. GRANT NUMBER**<br>**5c. PROGRAM ELEMENT NUMBER** |
| **6. AUTHOR(S)**<br>Wilson, Paul P., Captain, USAF | **5d. PROJECT NUMBER**<br>**5e. TASK NUMBER**<br>**5f. WORK UNIT NUMBER** |

| **7. PERFORMING ORGANIZATION NAMES(S) AND ADDRESS(S)** | **8. PERFORMING ORGANIZATION REPORT NUMBER** |
|---|---|
| Air Force Institute of Technology<br>Graduate School of Engineering and Management (AFIT/ENY)<br>2950 Hobson Way, Building 640<br>WPAFB OH 45433-8865 | AFIT-ENY-MS-19-M-253 |

| **9. SPONSORING/MONITORING AGENCY NAME(S) AND ADDRESS(ES)** | **10. SPONSOR/MONITOR'S ACRONYM(S)** |
|---|---|
| AFLCMC/EB<br>207 West D Ave, Bldg 349<br>Eglin AFB, FL 32542<br>850-883-3277 and David.liu@us.af.mil<br>ATTN: Maj David Liu | **AFLCMC/EB** |
| | **11. SPONSOR/MONITOR'S REPORT NUMBER(S)** |

**12. DISTRIBUTION/AVAILABILITY STATEMENT**
**DISTRUBTION STATEMENT A.** APPROVED FOR PUBLIC RELEASE; DISTRIBUTION UNLIMITED.

**13. SUPPLEMENTARY NOTES**
This material is declared a work of the U.S. Government and is not subject to copyright protection in the United States.

**14. ABSTRACT**

This research analyzes the performance of a nominal air-to-air tactical missile with varying configurations of wire-embedded end-burning solid propellant grains. Single and multi-wire models are developed to determine if total impulse and range is improved. Discontinuities in the wires are simulated to determine if gaps in the wire will affect overall performance. Five wire materials, seven wire diameters, and nine different break locations are tested. This research demonstrates wire discontinuities have negligible impact on performance and carbon nanotube fibers can theoretically improve total impulse by up to 25% compared to radially burning boost-phase grains while providing similar thrust outputs.

**15. SUBJECT TERMS**
Rocket Propulsion, Solid Propellant, Heat Transfer, Numerical Methods, Wired Propellant

| **16. SECURITY CLASSIFICATION OF:** | | | **17. LIMITATION OF ABSTRACT** | **18. NUMBER OF PAGES** | **19a. NAME OF RESPONSIBLE PERSON** |
|---|---|---|---|---|---|
| **a. REPORT** | **b. ABSTRACT** | **c. THIS PAGE** | | | Dr. Carl R. Hartsfield, PhD, AFIT/ENY |
| U | U | U | UU | 118 | **19b. TELEPHONE NUMBER** *(Include area code)*<br>(312) 785-3636, ext 4667<br>(carl.hartsfield@afit.edu) |

**Standard Form 298 (Rev. 8-98)**
Prescribed by ANSI Std. Z39-18